

# Combined EBSD and Computer-Assisted Quantitative Analysis of the Impact of Spark Plasma Sintering Parameters on the Structure of Porous Materials



SZYMON NOSEWICZ, GRZEGORZ JURCZAK, WITOLD CHROMINSKI,  
JERZY ROJEK, KAMIL KASZYCA, and MARCIN CHMIELEWSKI

The paper presents the experimental, numerical, and theoretical investigation of the microstructure of nickel aluminide samples manufactured by spark plasma sintering using electron backscatter diffraction and computer assisted software. The aim of the work was to reveal the evolution of the microscopic and macroscopic parameters related to the microstructure of the material and its dependence on the applied sintering parameters—temperature and pressure. The studied porous samples with different relative density were extracted from various planes and then tested by electron backscatter diffraction to evaluate the crystallographic orientation in every spot of the investigated area. On this foundation, the grain structure of the samples was determined and carefully described in terms of the grain size, shape and boundary contact features. Several parameters reflecting the grain morphology were introduced. The application of the electric current resulting in high temperature and the additional external loading leads to the significant changes in the structure of the porous sample, such as the occurrence of lattice reorientation resulting in grain growth, increase in the grain neighbours, or the evolution of grain ellipticity, circularity, grain boundary length, and fraction. Furthermore, the numerical simulation of heat conduction *via* a finite element framework was performed in order to analyse the connectivity of the structures. The numerical results related to the thermal properties at the micro- and macroscopic scale—local heat fluxes, deviation angles, and effective thermal conductivity—were evaluated and studied in the context of the microstructural porosity. Finally, the effective thermal conductivity of two-dimensional EBSD maps was compared with those obtained from finite element simulations of three-dimensional micro-CT structures. The relationship between the 2D and 3D results was derived by using the analytical Landauer model.

<https://doi.org/10.1007/s11661-022-06821-z>  
© The Author(s) 2022

## I. INTRODUCTION

**SINTERING** is a complex physical and chemical process that is thermally activated, leading to the connection of loose particles into a bulk structure as a

result of mass transfer mechanisms.<sup>[1]</sup> One of the most novel sintering approaches aimed at materials densification from a powder mixture is the spark plasma sintering (SPS) method.<sup>[2–4]</sup> In this technique, a direct electric current flow is used to heat the powders and die and a uniaxial mechanical load/pressure is applied to simultaneously accelerate its densification.<sup>[5]</sup> It should be stated that the most important advantages of the SPS method are: (i) possible densification of various material types (with various chemical bondings and electric conductivities), (ii) short exposure times in high temperatures, (iii) limitation of the grain growth, and (iv) restriction of inexpedient reactions, and thus, the formation of the undesirable phases and products is eliminated.<sup>[6]</sup>

Due to the several benefits, the SPS technique seems to be very attractive, but it is also complex and not entirely predictable.<sup>[7]</sup> The relationship between the sintering conditions and their effect on the

---

SZYMON NOSEWICZ, GRZEGORZ JURCZAK, and JERZY ROJEK are with the Institute of Fundamental Technological Research, Polish Academy of Sciences, 5B Pawinskiego, 02-106 Warsaw, Poland. Contact e-mail: snosew@ippt.pan.pl WITOLD CHROMINSKI is with the Faculty of Materials Science and Engineering, Warsaw University of Technology, 141 Woloska Str, 02-507 Warsaw, Poland. KAMIL KASZYCA and MARCIN CHMIELEWSKI are with the Lukaszewicz Research Network, Institute of Microelectronics and Photonics, 133 Wolczynska Str, 01-919 Warsaw, Poland.

Manuscript submitted June 14, 2022; accepted September 1, 2022.

microstructural changes is among the primary topics in powder metallurgy research.<sup>[8]</sup> The knowledge of the microstructural parameters and their effect on the physical behaviour of nonhomogeneous sintered materials is crucial to predict or intentionally tailor the microstructure for the desired mechanical<sup>[9]</sup> or thermal properties.<sup>[10]</sup>

A precise description of such a complicated sintered structure requires specific and advanced tools, both numerical and experimental. Numerical simulations at the microscopic level may provide an alternative tool for the determination of macro- and microscopic properties of a sintered material,<sup>[11]</sup> however, hardly any work on the simulation of SPS processes at the microscopic level can be found. The current state of the particle-based modelling of the SPS process attempts to model the thermo-electromechanical process at the particle/grain level and existing models are based on quite simplistic assumptions.<sup>[12]</sup>

Recently, scanning electron microscopy (SEM) with particular reference to its enhancement using electron backscatter diffraction (EBSD) seems to be the most popular technique to analyze the microstructure of nonhomogeneous materials experimentally.<sup>[13,14]</sup> Voids and pores within the structure can be easily identified by the band contrast parameter of EBSD maps.<sup>[15,16]</sup> Moreover, the EBSD technique can be applied to study the link between the sintering conditions and the properties of particle and grain boundaries at the microscopic level affecting significantly the macroscopic properties of the sample.<sup>[17,18]</sup> Mapping the local crystallographic orientation, identifying the grain boundary networks, as well as calculating the microstructure statistics (*e.g.*, pore/particle fraction, grain boundary density) performed by the EBSD technique allows for a better insight into the properties of the sintered material.<sup>[19]</sup> By applying the EBSD analysis coupled with the appropriate software, Bobrowski *et al.*<sup>[20]</sup> reconstructed the grain boundary networks and calculated the grain boundary density of sintered zirconia. A comparison of the structural morphology between the initial powder and sintered material was conducted by Matuła *et al.*<sup>[21]</sup> Then, in addition to standard grain size statistics based on EBSD measurements, Liang *et al.*<sup>[22]</sup> showed that the particle aspect ratio distribution was very important for investigating Si<sub>3</sub>N<sub>4</sub> ceramics due to its thermal conductivity anisotropy. Machio *et al.*<sup>[23]</sup> performed EBSD measurements of the phase composition, crystal structures, and grain orientations of sintered Ti based alloys. Finally, Xia *et al.*,<sup>[24]</sup> on the basis of a series of 2D EBSD images, reconstructed the 3D structure with grain-pore interfaces, pore connectivity, and tortuosity.

Basically, backscattered electrons carry much more information about the structure, *e.g.*, crystallographic orientation or phase, so we are able to distinguish between grains or phases within the sample, identify interfaces, *etc.*<sup>[25,26]</sup> Different from micro-computed tomography (micro-CT),<sup>[10,27,28]</sup> EBSD allows determining effectively several microstructural parameters, such as grain geometry, particles and voids, grain-grain interfaces (boundary), grain morphology within particles or/and grains misorientation. Despite several

advantages of the proposed methodology, EBSD investigation of sintered materials suffers also from a few limitations and deficiencies, such as the locally insufficient quality of the prepared sample surface (especially in the case of brittle and porous materials) and, hence, the several unsolved spots of the sample surface during the EBSD analysis, which may interfere the real representation of material microstructure. However, EBSD is typically a 2D experiment, as it scans surfaces, thus it limits the complete overview of the sample. By cross-section milling using a focused ion beam, it is possible to obtain progressive 2D images of the sample. Such a concept is used by three-dimensional electron backscatter diffraction (3D-EBSD or FIB-SEM).<sup>[15,29]</sup>

A large quantity of generated data related to the microstructure obtained by modern imaging techniques such as EBSD and micro-CT may demand automatic reconstruction algorithms based on image processing techniques to recognize structure patterns, *e.g.*, analysis of EBSD maps to recognize phases.<sup>[30,31]</sup> However, image artefacts typical of porous sintered materials depicted *via* scanning electron microscopy requires attention, hence the automation reconstruction is quite challenging.<sup>[32]</sup> A popular approach is based on the analysis of structure images with 2D or 3D reconstruction coupled with a numerical simulation to evaluate the effective physical properties of the material, *e.g.*, image-based finite element modelling (FEM),<sup>[19]</sup> micro-CT FEM,<sup>[33]</sup> or EBSD-based FEM.<sup>[34]</sup>

The presented work aims to characterize a porous structure sintered by the SPS technique at various conditions and then reconstructed by EBSD mapping. Based on the advantageous capabilities of the EBSD approach, presented in previous paragraphs, we evaluated and analysed both macro- and microscopic parameters of sintered samples, such as global surface fraction, grains size, shape and their contact and boundary features which are essential in the context of process optimization and the description of material in the most accurate way. The quantitative analysis of the structural features of the grain morphology has been carried out by own software supported by a non-commercial one. Finally, the numerical analysis is devoted to highlight the impact of the material state on the microstructure connectivity reflected in the form of thermal conductivity. The general scope of the paper is shown in Figure 1.

## II. METHODOLOGY AND PROCEDURES

### A. Experimental Techniques—Manufacturing and EBSD Mapping

As a representative material for the experimental and numerical investigation, intermetallic NiAl powder (Goodfellow, purity 99.9 pct, gas atomised) was selected and sintered *via* the SPS method. Intermetallic NiAl compounds are characterized by a very attractive combination of physical and mechanical properties.<sup>[35]</sup> Except for the high melting point, low density and high oxidation resistance at high temperatures, they also have a high modulus of elasticity. Especially, Ni–Al based

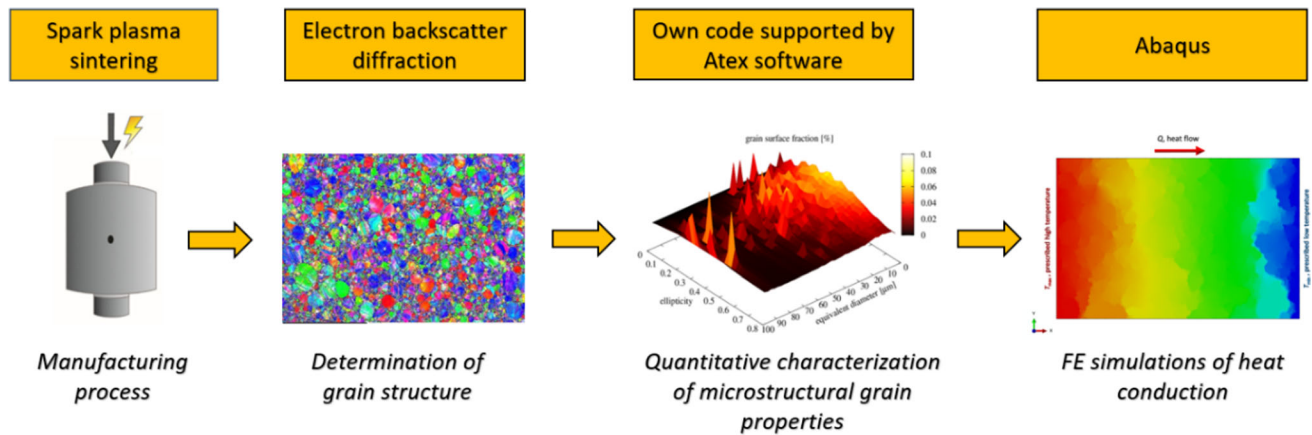


Fig. 1—General scope of applied methodology.

compounds are resistant to oxidation even up to 1000 °C, but also have high tensile and compressive strength (even at high temperatures), high fatigue strength, high creep strength, good abrasion resistance, and good thermal and electrical conductivity. Due to the several advantageous properties, the technologies of their manufacturing are of great importance. The presented work is in line with the current trends of advanced materials production efficiently, incl. by using the SPS technique.

Figure 2 shows the scheme of the SPS apparatus. The powder was placed in the graphite die inside a vacuum chamber (the absolute pressure was less than  $5 \times 10^{-3}$  mBar) and sintered *via* the heating programs. The first sintering stage (maintaining at 200 °C for 15 minutes) is applied for the purification of the NiAl powder from gases and water. After that, the system is heated up to a sintering temperature (1100 °C, 1200 °C, 1300 °C) with a heating rate of 100 K/min and the final pressure is applied (5 or 30 MPa). At the sintering stage, the sample is maintained at the declared temperature and pressure for 10 minutes, and after that, the power is switched off and the system is allowed to cool freely.

In the SPS process, the powder particle surfaces are more easily purified and activated than in conventional sintering processes, and material transfers at both the micro and macro levels are promoted, so a high-quality sintered compact is obtained at a lower temperature and in a shorter time than with conventional processes.<sup>[7]</sup> The discussion about the mechanisms responsible for the densification *via* SPS method is still open. Two mechanisms, the Joule heating effect and an electrical field diffusion effect, seem to play the most crucial roles and are not debated (Figure 2). In the SPS method, the die and punches (typically made of graphite) are heated by Joule heating from a current passing through them. The major part of the Joule heat is generated in the graphite elements, which act as an efficient heat source in direct contact with the powders.<sup>[8]</sup> As the result of the flow of electric current, individual particles of powders are bonded under the conditions of mechanical pressure (Figure 2). Unlike the conductive heat transport that takes place during conventional

sintering, the volume heating resulting from the Joule effect enables a rapid increase in the temperature (up to 2000 °C with rates up to 10 K/s), which influences the mass transport mechanisms responsible for the sintering phenomenon<sup>[36]</sup> and enables the grain growth to be controlled.

After the manufacturing process, the sintered NiAl samples were tested in the context of their densification because they were manufactured by the application of various combinations of SPS process parameters. Their bulk density was evaluated using the hydrostatic method, which is based on the Archimedes' principle. The degree of densification was presented by the relative density,  $\rho^{\text{exp}}$ , defined as the ratio of the measured bulk density and the theoretical density of the NiAl material ( $\rho^{\text{theo}} = 5.91 \text{ g/cm}^3$ ).

Next, the samples were devoted to electron backscatter diffraction testing. Generally, due to its two-dimensional nature, the EBSD technique suffers from a limited amount of data obtained from the analysis of a single surface, as we compare it to 3D testing, such as micro-CT.<sup>[10]</sup> To study the effect of various planes to direction of the electric current and the external pressure application on the structural features of the EBSD maps (see Figure 2), the sample surfaces were extracted from perpendicular (samples 1, 3, 4, and 6) and parallel planes (samples 2 and 5). Such distinction allows us to obtain a better overview of the sample's microstructure and grain properties.

The EBSD measurements were performed on mechanically polished surfaces. A short-time  $\text{Ar}^+$  ion polishing was utilized just before the measurements to improve the signal. Particular care was taken for the surface preparation, as unresolved points are an important factor in this study; thus, it was crucial to minimize their number resulting from the poor signal from the grain interiors.

An analytical field emission SEM Hitachi SU70 equipped with an HKL Nordlys EBSD detector was used in this study, and the acceleration voltage was set to 20 kV. Maps were gathered with the use of a square grid of points separated by 1  $\mu\text{m}$ .

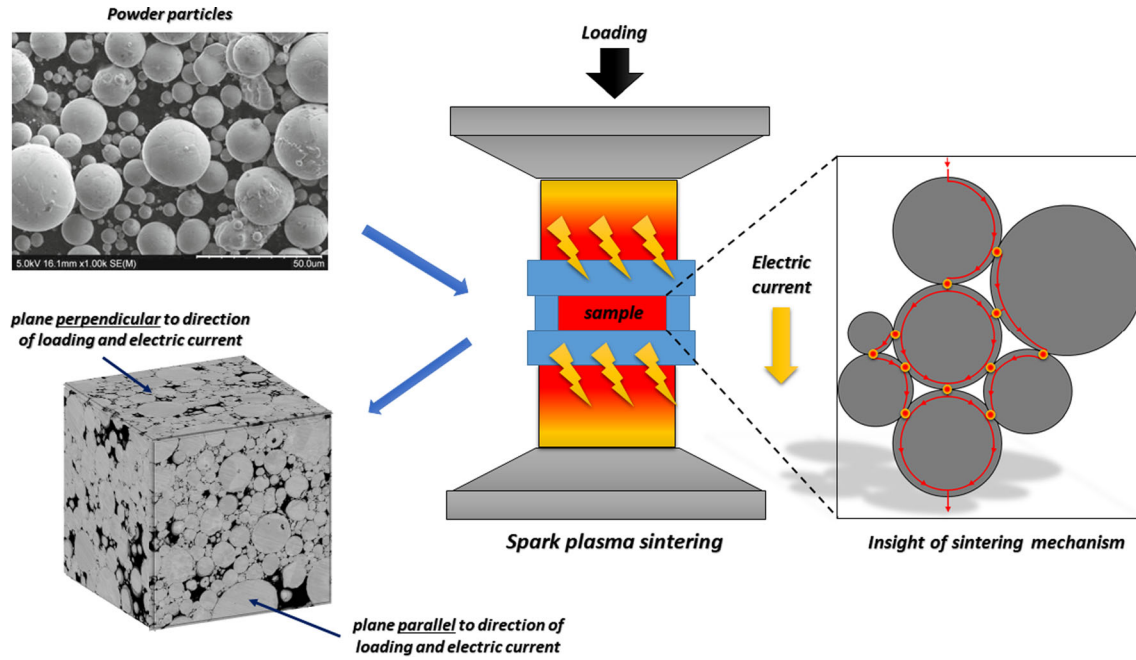


Fig. 2—Scope of the manufacturing process of NiAl samples by spark plasma sintering.

### B. Evaluation of the Microstructural Grain Properties

The determined orientation results were next processed by our own code written in C# supported by the ATEX program, a non-commercial software aimed at the analysis of data obtained by backscattered electron and X-ray diffraction.<sup>[37]</sup> Based on the software functionality, it was possible to create the map of pixels representing the sample structure. Neighbouring pixels with a particular corresponding orientation were locally grouped, and as a consequence, the grain object was composed. Unsolved spots with non-orientation data were treated as void/gaps representing the material porosity. In several cases, such non-indexed pixels can be found within the grain body; thus, a couple of map correction approaches based on noise reduction and spike correction were employed in order to fill the voids. The noise reduction strategy aims to assign an orientation to non-indexed pixels in two steps.<sup>[37]</sup> In the first one, the non-indexed pixels surrounded by eight indexed pixels displaying a misorientation of less than 3 deg are indexed by the mean orientation of neighbors. Several loops are performed, until all non-indexed pixels are corrected. Second, the procedure is repeated with decreasing number of neighbours. The procedure is stopped when all the non-indexed pixels have been corrected. The spike correction strategy is based on similar assumptions. The spikes displaying at least seven indexed neighbour pixels misoriented by less than 3 deg are re-oriented by the mean orientation of those 7 or 8 neighbour pixels. One or two loops can be set by the user. The procedure is limited to two loops to avoid important changes to the original map.

The grain structure, represented as the collection of indexed pixels, was characterized by several microscale parameters. Knowing the unit size of the pixel (1  $\mu\text{m}$ )

and the pixel number assigned to each grain, we were able to calculate its *grain surface area*  $A$  and, hence, its size as *the equivalent diameter*  $d^{\text{eq}}$ , defined as the diameter of the equivalent circle area:

$$d^{\text{eq}} = 2\sqrt{A/\pi}. \quad [1]$$

One of the most important quantities, while simultaneously being the main effect of spark plasma sintering, is the densification level of the sintered material. In the case of such a 2D analysis, it can be represented as the *global surface fraction*,  $\rho$ , calculated as the ratio of the total number of grain areas occupied and the known total area of the image  $A^{\text{img}}$ :

$$\rho = \frac{\sum_i^{n_{\text{tot}}^{\text{gr}}} A_i}{A^{\text{img}}}, \quad [2]$$

where  $i$  is the number of grains and  $n_{\text{tot}}^{\text{gr}}$  is the total number of grains in the EBSD map.

Once the grains were detected and their gravity centres and size were known, they were characterized by their shape features. Generally, there are many approaches to describe the compactness or roundness of an object.<sup>[38]</sup> In order to study the effect of the SPS process by application of an external pressure and high sintering temperature on the grain shape, two parameters, the *ellipticity*  $E$  and *circularity*  $C$ , were selected. The first one provided information of whether the shape of the grain indicates a more circular form (close to 0) or more elliptical form (close to 1). Here, the grain object was fitted by ellipses. From the fit, the big axis  $a$  and the small axis  $b$  as well as the angle of the big axis with the direction 1 of the sample were obtained.<sup>[37]</sup> Thus, the ellipticity of each grains is calculated as follows:

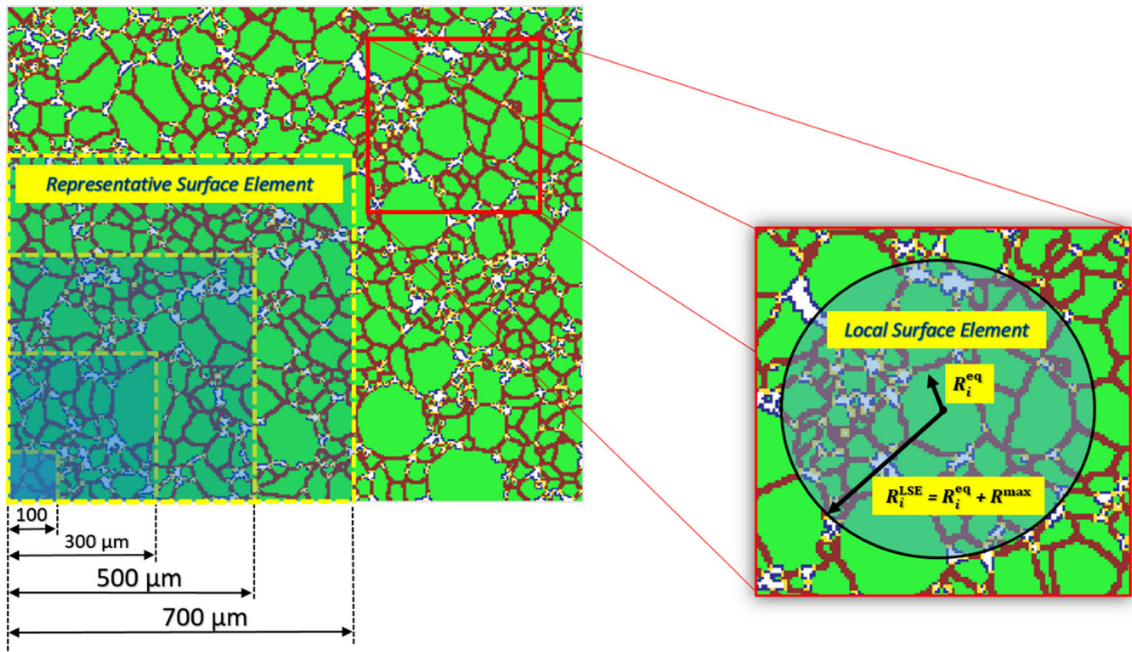


Fig. 3—The concept of representative surface element (RSE) and local surface element (LSE) (Color figure online).

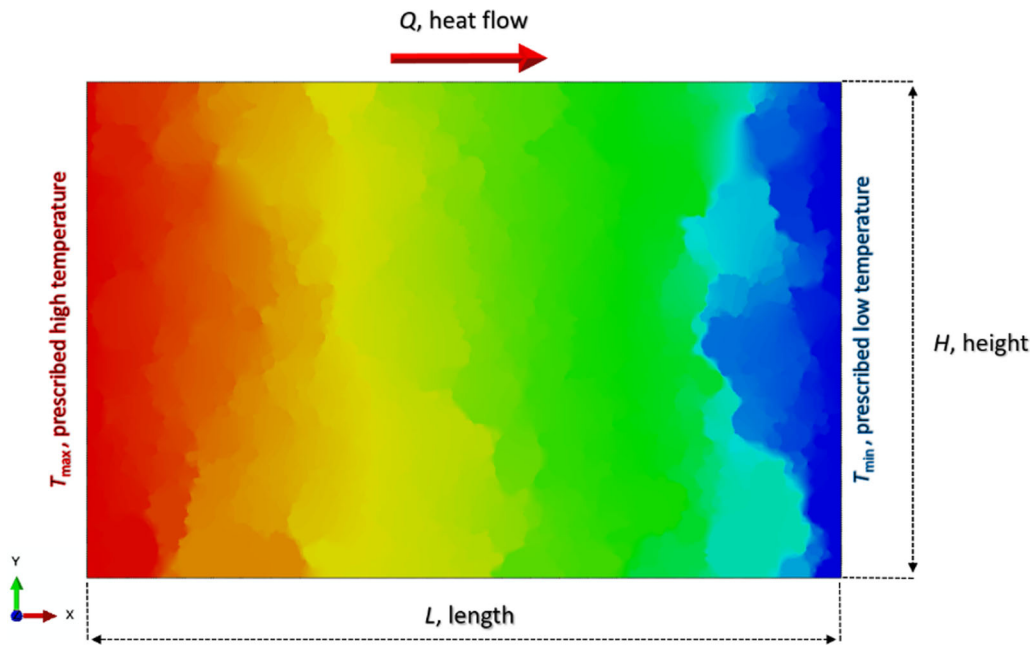


Fig. 4—Setup of the EBSD-based finite element simulation of heat conduction.

$$E = 1 - \frac{b}{a}. \quad [3]$$

$$C = \frac{4\pi A}{P^2}. \quad [4]$$

The second selected shape factor, the circularity, exhibits the complexity of the shape of the grain object, comparing the perimeter of a shape  $P$  to the area it contains. It approaches 1 as the grain indicates a more circular and compact shape. Circularity can be estimated by the following formula:

Circularity is sensitive to small scale objects that indicate an increased perimeter compared to the corresponding object area. To minimize such unfavourable effects, the circularity study was performed only for medium and large-size grain fractions. Moreover, the

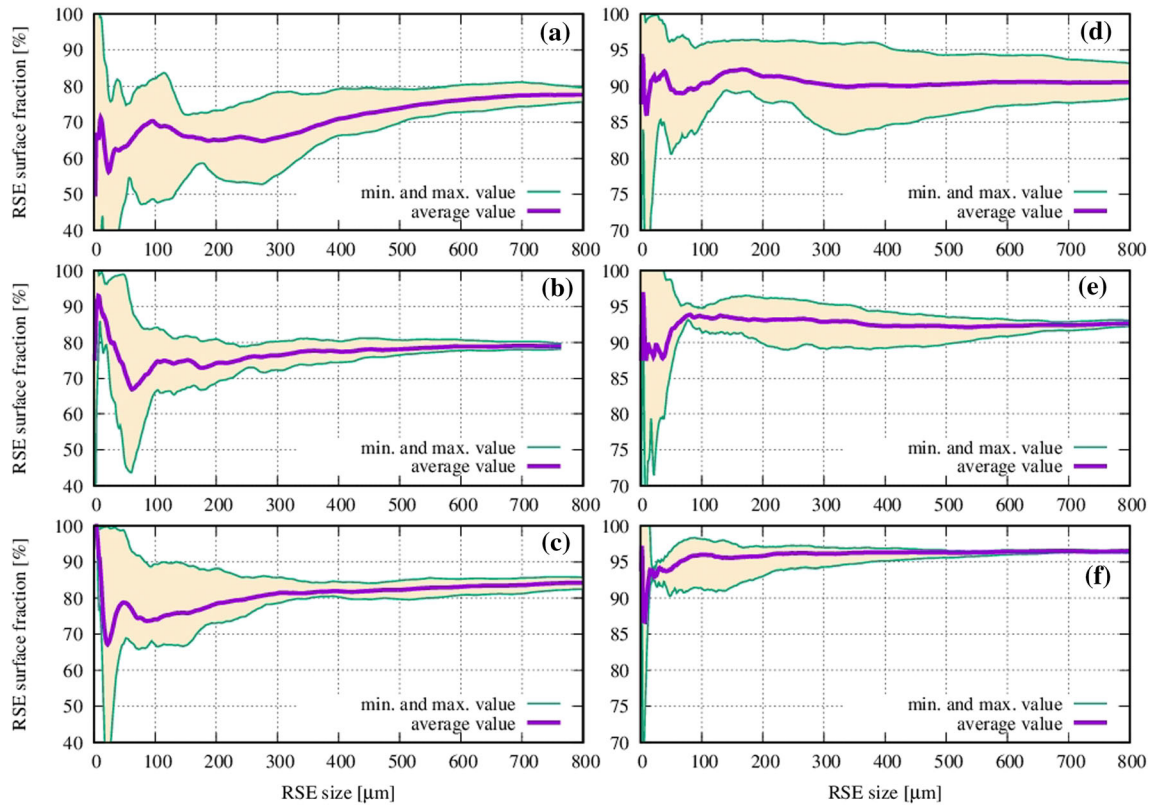


Fig. 5—Surface fraction of RSE vs RSE size of the sample: (a) 1-(1100 °C, 5 MPa), (b) 2-(1200 °C, 5 MPa), (c) 3-(1300 °C, 5 MPa), (d) 4-(1100 °C, 30 MPa), (e) 5-(1200 °C, 30 MPa), and (f) 6-(1300 °C, 30 MPa).

statistical data of both shape factors were presented in the form of the weighted arithmetic mean with weights corresponding to grain diameters.

The grain perimeter, being a major factor of the circularity parameter, was calculated as a sum of the outer pixels that were in contact with the pixels of the other grain or with non-indexed pixels (pores). In the first case, such pixels create a grain boundary, and hence, these two grains are called “*first neighbours*”. The level/degree of the contact of neighbours sharing a common boundary can be evaluated by the *grain boundary length*  $l^{gb}$  and the *grain boundary fraction*  $f^{gb}$ . The former is the sum of pixels of single contact between two grains. The latter can be defined as the single grain property as the ratio of the sum of all contacts with other grains with  $l_{gb}$  and the perimeter:

$$f^{gb} = \frac{\sum_i^{n^c} l_i^{gb}}{P}, \quad [5]$$

where  $i$  is the number of neighbour  $f$  a single grain and  $n^c$  is the total number of contacts/neighbours of a single grain.

In other words, the grain boundary fraction answers the question of the extent to which a single grain is surrounded by neighbouring grains. An example of the grain structure with its several features can be seen in Figure 3. The green colour demonstrates the interior of the grains, and the red colour indicates the grain boundaries. The void–grain interface is represented by

the blue colour, and the pixels exhibiting both the boundary with the other grain and void are shown in yellow. Finally, the white colour demonstrates the voids and porosity.

Here, an important issue related to the definition of grain contacts should be discussed. Basically, sintered powder particles constituting the porous structure at the macroscopic scale are bonded by necks. The distinction between grain boundaries and necks on EBSD maps is not so obvious, as the former can generally be defined as the connection between grains and the latter can be defined as the connection between particles, which in many cases are the clusters of small grains (see Figure 2—image with powder particles). Because EBSD does not offer the tool to identify the single particle body, all contacts between pixels with different orientations are treated as the grain boundaries wherever they connect the various grains or particles.

With this in mind, we evaluated the coordination number  $N$ , defined as the average number of contacts per particle, which is calculated as follows<sup>[39]</sup>:

$$N = \frac{2n_{tot}^c}{n_{tot}^{gr}}, \quad [6]$$

where  $n_{tot}^c$  is the total number of contacts between the  $n_{tot}^{gr}$  grains. Moreover, we calculated the weighted coordination number  $N^w$  with weights corresponding to grain diameters.

In order to study the pixel map efficiently corresponding to the real representation of the NiAl grain structures, the global surface fraction of the EBSD data should correspond well to the experimental relative density. Because the densification level is the major indicator of the properties of porous materials,<sup>[40]</sup> the assessment of the representativeness of the EBSD data with the determination of the proper size of the representative surface element (RSE) seems to be a crucial issue. The concept of the determination of an adequate RSE size is presented in Figure 3. It considers the calculation of the surface fraction,  $\rho^{\text{RSE}}$ , within the square-shape RSE along with increasing its size. The test was initiated in four corners of each map, giving more statistical data. As the  $\rho^{\text{RSE}}$  stabilizes, *i.e.*, the fluctuation of parameter in the function of RSE size is definitely reduced, the relevant RSE size is found.<sup>[10]</sup>

Along with the RSE study, the homogeneity of the structure was checked by application of local surface element (LSE). It aims to study the material densification at the microscopic level using the local surface fraction,  $\rho^{\text{LSE}}$ , within the circular-shape domain (Figure 3), similar to the approach reported in Reference 41. LSE is placed in the centres of mass of each grain with a radius  $R^{\text{LSE}}$ , defined as the sum of the equivalent grain radius  $R^{\text{eq}}$  and the maximum radius of grain found within whole map,  $R^{\text{max}}$ . In that way, the difference in the local density within the map structure can be evaluated, which allows the material homogeneity at the macroscopic scale to be assessed.

### C. EBSD-Based Finite Element Framework of Heat Conduction

The final investigation of the obtained EBSD structures was performed by means of the finite element simulations of heat transfer. The main purpose of numerical modelling is to characterize the NiAl maps by several parameters related to heat conduction at the microscopic scale, such as the magnitude of local heat fluxes  $q$  and the deviation angle  $\beta$ . The former can be defined as the directional variation of the  $\vec{q}$  vector with respect to the central axis of heat flow.<sup>[10]</sup> The proposed thermal analysis can be treated as the complementary study of the sintered NiAl microstructure. The determined structural features, especially the grain contacts and boundaries, were combined with the results from the numerical simulation. Moreover, by introducing the macroscopic parameter effective thermal conductivity  $\lambda_{\text{eff}}$ , we tend to describe the global performance of the 2D sintered structure in the context of material integrity, connectivity, and thermal capacity, as well as in References 42 through 45. The investigated 2D conductivity may represent a useful lower limit of the real 3D conductivity.<sup>[45]</sup> Finally, keeping in mind the limitations of 2D simulations, we took advantage of our recent work regarding the thermal conductivity of 3D NiAl structures obtained by micro-CT analysis.<sup>[10]</sup> Thus, the comparison of 2D EBSD-based and 3D micro-CT based FEM results of heat transfer seems to be an intriguing matter.

To describe the heat flow through the material and transfer *via* the conduction mechanism driven by a temperature gradient, a Fourier's law is usually employed. It assumes the heat flux  $q$  is proportional to the temperature gradient  $\Delta T$ . In the case of a rectangular 2D sample, we have heat flow limited only to one direction, so we may present the one dimensional heat flow in the form:

$$q = -\lambda \frac{\Delta T}{L}, \quad [7]$$

where  $L$  is the length of the body. The proportionality coefficient  $\lambda$  is called the thermal conductivity of the material. Heat flow occurs from the hot side to the cold side (Figure 4); therefore, a minus sign appears in the equation.

Pores filled with gas/air with orders of magnitude lower conductivity are obstacles for heat transfer and force the heat flux to meander. Therefore, heat flow in the porous material is highly dependent on the porosity of the material. Because modelling of a porous material is rather complicated and precise mapping of the porosity is required for adequate results, we may use global and macroscopically averaged thermal conductivity that takes into account the effective thermal properties of the sample. To describe the averaged thermal conductivity of a porous material, we use the effective thermal conductivity  $\lambda_{\text{eff}}$ , which describes the generalized thermal properties of the heterogeneous material. Therefore, the effective thermal conductivity coefficient in a 2D sample  $\lambda_{\text{eff}}^{2\text{D}}$  with height  $h$  (Figure 4) can be calculated as follows:

$$\lambda_{\text{eff}}^{2\text{D}} = -\frac{QL}{\Delta Th}, \quad [8]$$

where  $Q$  is the linear density of the heat.

Generally, there are several analytical models for determining the  $\lambda_{\text{eff}}$  of porous materials.<sup>[46]</sup> Among the many theoretical approaches and assuming various solid and pore shapes and spatial distributions (parallel, series, Maxwell-Eucken, and so on), the Landauer model based on the effective medium percolation theory<sup>[47]</sup> has become one of the most suitable analytical approaches for evaluating  $\lambda_{\text{eff}}$ .<sup>[43,48-51]</sup> The effectiveness of the Landauer relation stems from the fact that it assumes a completely random distribution of all the components.<sup>[46]</sup> It is defined as follows:

$$\lambda_{\text{eff}} = 0.25 \left[ \lambda_p (3v_p - 1) + \lambda_s (2 - 3v_p) + \left\{ [\lambda_p (3v_p - 1) + \lambda_s (2 - 3v_p)]^2 + 8\lambda_s \lambda_p \right\}^{0.5} \right] \quad [9]$$

where  $\lambda_s$  is the thermal conductivity of the solid,  $\lambda_p$  is the thermal conductivity of the pores, and  $v_p$  is the pore volume fraction.

Because we consider a heterogeneous material with two components with significantly different properties, *i.e.*,  $\lambda_s \gg \lambda_p$ , the Landauer relation can be reduced to the following form:

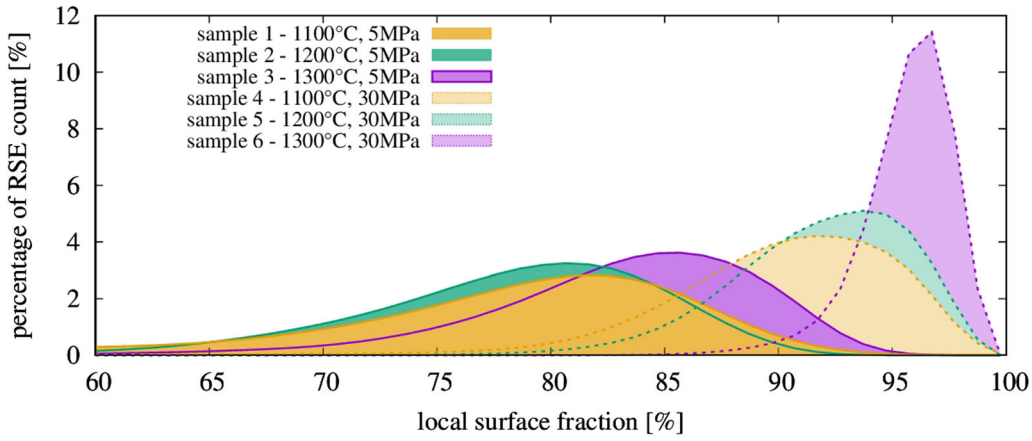


Fig. 6—The distribution of the local surface fraction of LSE  $\rho^{\text{LSE}}$  for the sintered samples.

$$\lambda_{\text{eff}} = 0.5\lambda_s(2 - 3v_p). \quad [10]$$

The main drawback of the theoretical models, including the Landauer relation, is the relatively far-reaching simplification of the non-homogeneous geometry of the phases, see for example Reference 52. Therefore, the usability of these models is sometimes limited only to specific materials with a regular and predictable microstructure. In reality, the microstructure of a non-homogeneous material can also be described by the spatial distribution of the phases, geometry of the particle boundaries, and their quality (*via* interfacial thermal resistance<sup>[10,52]</sup>) and may strongly affect the macroscopic heat flux and, therefore, the evolution of the  $\lambda_{\text{eff}}$  coefficient value of the sample. In terms of the adequacy of thermal conduction, the detailed knowledge of the microstructure seems to be essential, as it allows us to reconstruct the real material and perform the necessary numerical simulation.

In this work, the effective thermal conductivity  $\lambda_{\text{eff}}^{2\text{D}}$  of the 2D representation of the NiAl structure was calculated based on the real structure obtained from EBSD imaging. The real microstructure of the sample is repeated within the FE mesh by identifying the type of material (grain/pore). Firstly, the EBSD image of the porous structure was transformed, pixel by pixel, into the 2D FE mesh. Each pixel of the EBSD image corresponds to the DC2D4 (4-node quadrilateral linear heat transfer) finite element. As we used direct transformation “pixel-to-element”, the accuracy of the finite element mesh corresponds explicitly to the resolution of the EBSD technique. Hence, in this case, EBSD resolution and finite element size are equal to 1  $\mu\text{m}$ . The final size of FE mesh has been taken on the basis of the size of EBSD maps ( $\sim 1000 \times 1500$  pixels).

The heat flow through the samples was calculated in both directions (X and Y), and the results of  $\lambda_{\text{eff}}^{2\text{D}}$  were averaged. Temperature (boundary conditions) has been set at consecutive horizontal and vertical opposite ending edges of the sample and were set as 0 and 100 °C, respectively, for the cold and hot edge. The side edges of the sample do not allow for heat flow;

therefore, we may assume that they fulfil the adiabatic behaviour. The thermal conductivity of NiAl was set to 88.5 W/m K, while for the pores, we assumed it was 0.05 W/m K. Heat fluxes through the sample were calculated by solving the thermal boundary-value problem for steady-state heat flow with the use of the Abaqus package incorporating heat conductivity routines.<sup>[53]</sup> The resultant distribution of nodal temperatures and heat fluxes allows for the calculation of the aggregated heat flow perpendicular to the cold edge and finally the calculation of  $\lambda_{\text{eff}}^{2\text{D}}$ , as stated in Eq. [8].

### III. RESULTS AND DISCUSSION

#### A. General Overview

On the basis of the methodology presented in Sections II–B and II–C, a comprehensive analysis of the sintered structures was carried out. Structural and thermal parameters related to grain size, shape, contacts, boundary and conductivity were determined for the whole set of grains of each map and are presented in Table I mostly as the averaged values with the standard deviation. The effect of sintering temperature and applied pressure on each grain parameter was studied and is discussed in the following Sections from III–B through III–G.

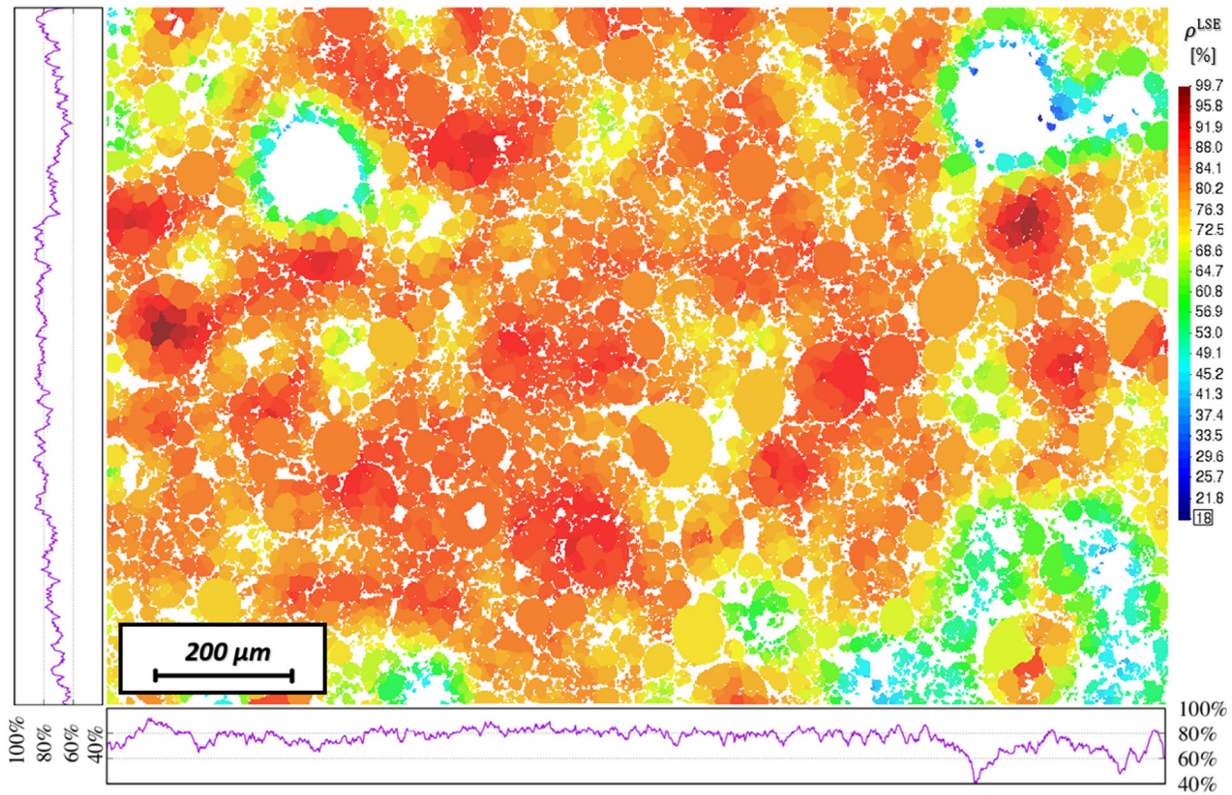
As seen in Table I, the global surface fraction grows with the increase in the sintering temperature and external pressure. The rather obvious pressure effect of compacting pressure on densification can be explained by the easier grain regrouping process at the early stage, intensification of diffusion processes under pressure, activation of diffusion flows, and finally, easier pore elimination at the final stage of sintering.<sup>[54]</sup> Moreover, the higher sintering temperature reduces the viscous resistance of interacting grains/particles and activates additional mass transport mechanisms, such as the grain boundary or volume diffusion.

It should be noted that the evaluated global surface fraction of the samples corresponds well with the experimental density results obtained by the Archimedes method shown in Table I. This result proved that despite

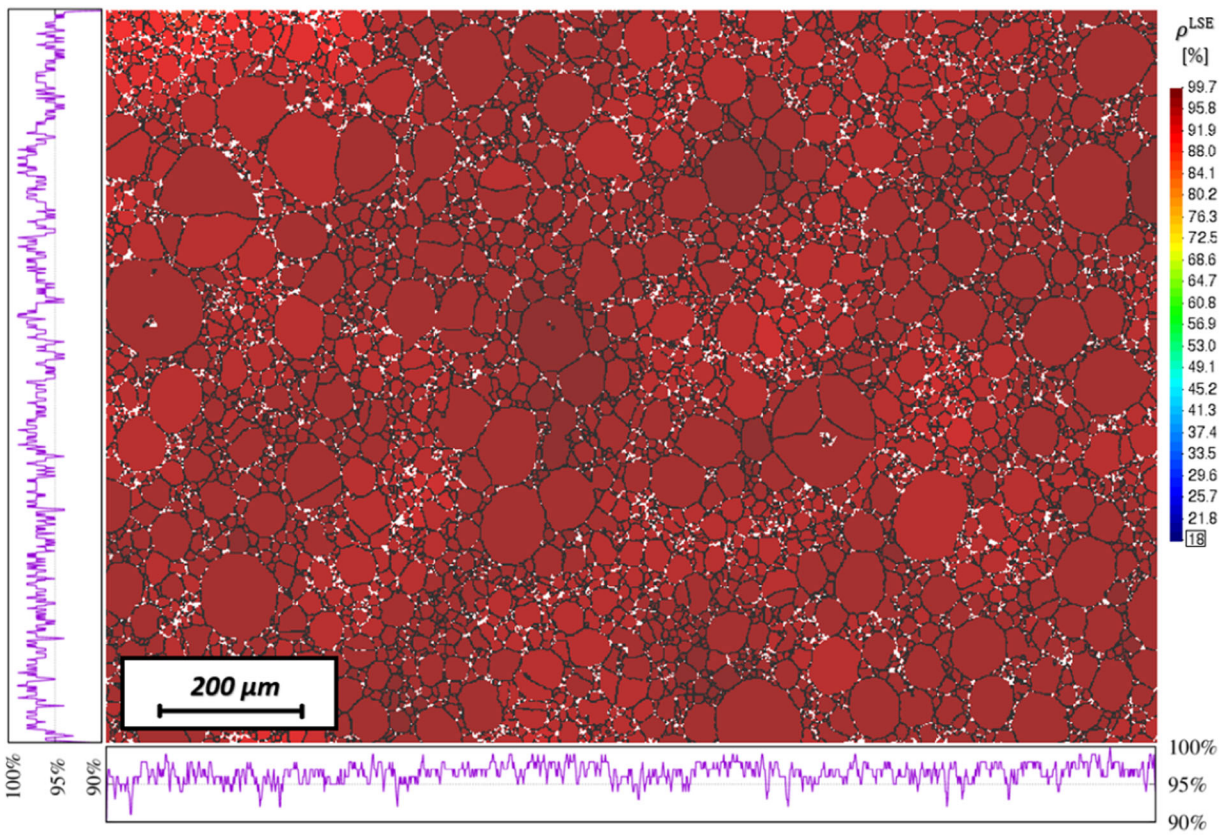


**Table I. Summary of Structural and Thermal Quantities Evaluated by the EBSD Image and the FEM Approach**

No. (Sintering Temp, Pressure)	Sample 1 (1100 °C, 5 MPa)		Sample 2 (1200 °C, 5 MPa)		Sample 3 (1300 °C, 5 MPa)		Sample 4 (1100 °C, 30 MPa)		Sample 5 (1200 °C, 30 MPa)		Sample 6 (1300 °C, 30 MPa)	
	Perpendicular		Parallel		Perpendicular		Perpendicular		Parallel		Perpendicular	
Considered Plane*	Perpendicular		Parallel		Perpendicular		Perpendicular		Parallel		Perpendicular	
Density/ Homogeneity	70.2		78.2		84.4		89.3		95.0		97.5	
experimental relative density, $\rho^{\text{exp}}$ [pct]	76.5		78.8		84.0		90.6		93.1		96.7	
global surface fraction, $\rho$ [pct]	77.0 ± 10		78.4 ± 6.2		83.4 ± 5.7		90.4 ± 5.2		92.2 ± 3.4		96.1 ± 1.5	
av. local surface fraction, $\rho_{\text{av}}^{\text{LSE}}$ [pct]	76.4 ± 7.8/		78.6 ± 4.8/		83.8 ± 5.1/		90.5 ± 3.8/		92.9 ± 2.1/		96.5 ± 1.3/	
av. pixel count along x/y dir. [pct]	76.3 ± 6.0		78.6 ± 4.4		83.8 ± 2.9		90.5 ± 2.1		92.9 ± 2.4		96.5 ± 1.2	
Size	10.3 ± 7.6		10.8 ± 9.0		13.4 ± 11.9		10.2 ± 5.9		9.1 ± 8.5		12.1 ± 11.9	
av. grain size, $d_{\text{av}}$ [ $\mu\text{m}$ ]	101.3		100.9		116.9		63.8		111.7		137.8	
max. grain size, $d_{\text{max}}$ [ $\mu\text{m}$ ]	0.24 ± 0.15		0.21 ± 0.15		0.16 ± 0.13		0.25 ± 0.16		0.33 ± 0.18		0.21 ± 0.14	
Shape	0.58 ± 0.13		0.63 ± 0.11		0.65 ± 0.13		0.63 ± 0.13		0.58 ± 0.13		0.58 ± 0.11	
weighted av. grain ellipticity, $E_{\text{av}}$	5918		5053		3315		8332		7635		4301	
weighted av. grain circularity, $C_{\text{av}}$	21,553		17,515		11,893		40,137		35,619		22,235	
eq. total grain number, $n_{\text{tot}}^{\text{gr}}$	7.3		7.0		7.2		9.7		9.4		10.4	
eq. total contact number, $n_{\text{tot}}^{\text{ct}}$	6.4		7.2		8.3		6.9		12.6		13.0	
coordinatation number, $N^{\text{w}}$	81,147		59,639		50,370		139,548		115,113		94,819	
eq. total grain boundary length, $l_{\text{tot}}^{\text{gb}}$ [ $\mu\text{m}$ ]	27.5		23.7		30.5		33.6		30.2		44.2	
av. grain boundary length, $l_{\text{av}}^{\text{gb}}$ [ $\mu\text{m}$ ]	48 ± 27		42 ± 25		44 ± 23		64 ± 25		66 ± 24		71 ± 22	
av. grain boundary fraction, $f_{\text{av}}^{\text{gb}}$ [pct]	2.1 ± 2.2		3.7 ± 2.8		3.7 ± 2.3		4.9 ± 1.7		5.2 ± 1.5		5.9 ± 1.0	
av. magnitude of heat flux, $q_{\text{av}}$ [ $\text{MW}/\text{m}^2$ ]	1.15		1.27		1.27		1.06		1.05		1.04	
$q_{\text{av}}^{\text{gb}}/q_{\text{av}}^{\text{gr}}$ ratio	30.2 ± 27.1		26.3 ± 25.3		23.8 ± 23.4		12.7 ± 16.2		10.1 ± 14.1		5.5 ± 9.3	
av. deviation angle of heat flux, $\beta_{\text{av}}$ [deg]	21.8		29.6		44.6		63.9		68.2		79.5	
effective thermal conductivity, $\lambda_{\text{eff}}^{2D}$ [ $\text{W}/\text{m K}$ ]												
Grain Boundary												
Thermal Properties												



(a)



(b)

Fig. 7—The map distribution of the local surface fraction  $\rho^{\text{LSE}}$  for: (a) sample 1 (1100 °C, 5 MPa) and (b) sample 6 (1300 °C, 30 MPa) with percentage content of grain pixel along the  $x$  (horizontal) and  $y$  (vertical) axis. The white color indicates the porosity.

the few deficiencies of the proposed methodology, such as the locally insufficient quality of the prepared sample surface and, hence, the several unsolved spots of the sample surface during the EBSD analysis, it can be an efficient tool for determining the global density of the structure.

### B. Homogeneity Study

The investigation of RSE of each of the six maps was performed *via* the procedure presented in Section II–B. The surface fraction of RSE was calculated along the increasing RSE size in order to check the balance moment of the results. The outcome of such an analysis is shown in Figure 5, where the average, minimum, and maximum values of the RSE surface fraction were evaluated for the six studied samples.

It was noticed that the stabilization of the average value of the RSE surface fraction depends on the sample; however, in all cases, it occurs before reaching the 800  $\mu\text{m}$  RSE size at the level of the global surface fraction for each sample (Table I). It proves that the determined EBSD maps constitute the valid representation of the porous microstructure because the sizes of the maps are bigger than the obtained final RSE sizes.

Furthermore, it can be stated that the applied higher external pressure (Figures 5(d) through (f)) decreases the RSE size while the results stabilize compared to the lower pressure (Figures 5(a) through (c)). The effect can be associated with the high particle rearrangement during the application of external loading that organizes the powder within the die just before the sintering process.<sup>[41]</sup> Hence, the resulting system of the particle powder after loading defines the position of powder particles and becomes the foundation of the sintered porous structure also after the spark plasma sintering.

Finally, the higher sintering temperature supports the reduction of the scatter of results. A relatively slight deviation of the minimum and maximum values of the RSE surface fraction of the samples sintered at 1200 °C and 1300 °C, especially for the bigger RSEs, apparently derives from the microstructural evolution and changes within the grain sizes and shapes along with the temperature rise. This aspect of the work will be discussed in Section III–C.

The second investigation concerning the homogeneity of the EBSD data was performed based on the methodology presented in Section III–B (Figure 3). The distributions of the local surface fraction  $\rho^{\text{LSE}}$  for all studied samples are shown in Figure 6. As the complementary results, the graphical distribution of  $\rho^{\text{LSE}}$  in the form of maps is presented in Figure 7 (for samples 1 and 6), and the average value  $\rho_{\text{av}}^{\text{LSE}}$  with the standard deviation is shown in Table I.

The results show the desirable consistency between the local distribution and global surface fraction for all samples. The average  $\rho_{\text{av}}^{\text{LSE}}$  corresponds well with the global one (Table I). As the global surface fraction grows, the scatter of  $\rho^{\text{LSE}}$  (standard deviation) decreases and the results are more consistent. This effect can be seen in Figure 6, where the wider distribution with the

low maximum peak indicates the larger scatter of the results and the less homogenous structure. The presented maps with  $\rho^{\text{LSE}}$  prepared with the distributions of the normalized grain pixel count along the  $x$  and  $y$  axis indicate a certain number of areas with a high porosity and a low value of  $\rho^{\text{LSE}}$ . These places can be characterized by a close vicinity to considerable voids (upper part of Figure 7(a)) remaining from the spark plasma sintering or from the preparation of the sample surface. Moreover, the low local surface fraction (up to 60 pct) can also be associated with a high number of pores with reduced size (bottom right part of Figure 7(a)).

This feature is also registered in the pixel content distributions provided with the maps where noticeable drops on the specific map positions (along the  $x$  and  $y$  direction) corresponding to such areas occurred. The pixel content of sample 1 shows a high fluctuation along the map axis, deviating significantly from the value corresponding to the global surface fraction and, hence, referring to the appreciable microstructural diversity. A nearly full dense structure of sample 6, in contrast to the porous sample 1, distinguishes itself in the high degree of homogeneity with small deviations of the pixel content and a fairly narrow distribution of  $\rho^{\text{LSE}}$  (Figures 6 and 7(b)).

### C. Grain Size

Besides the influence of spark plasma sintering on the macroscopic features such as the global surface fraction, it also significantly affects the microscopic structural parameters. The summary of the grain size parameters registered in Table I allowed us to conclude that there is a noticeable impact of the sintering temperature and a simultaneous low effect of the applied pressure. As the temperature increases, the average and maximum grain size grows in both processes of 5 and 30 MPa. The exception is sample 5, which has a reduced average grain size. This effect surely results from the fact that the map was obtained from parallel plane to external pressure application (Figure 2). Hence, the change in the grain geometry and size due to the compression effect should be mostly revealed here.

Apart from that, the moderate temperature effect is expected because the spark plasma sintering technique is introduced as the material manufacturing approach to reduce the grain growth during the process,<sup>[55]</sup> in contrast to more classical powder metallurgy methods such as hot pressing.<sup>[56]</sup>

More conclusions of the dependence of the grain size on the process parameters can be made from Figure 8. The distribution of the cumulative grain surface fraction was plotted for all studied samples. As the results grow with a high rate from the beginning and the curve gets flattened in the highest fraction, it indicates the large amount of the finest grains occupying the considerable area with a relatively low number of larger grains. An example of such a curve can be observed in the case of the samples sintered at a lower temperature (1100 °C). For a higher sintering temperature, the curves become more linear and flatten at the beginning compared to the

curves of lower temperatures. The larger fractions appear at the expense of the lower fractions. Moreover, a relatively good correspondence of the results for the same temperature and various pressures (samples 1 and 4, 2 and 5, 3 and 6) can be seen. This effect was confirmed by the distributions of the grain surface fraction presented in Figures 9(a) and (b).

The distributions of the samples sintered at 1100 °C and 5 and 30 MPa exhibit a similar shape with a large amount of the lower fraction of grains (up to 40 μm) occupying 87 pct (sample 1) and 97 pct (sample 4) of the total grain area. The mentioned issue can be seen in the

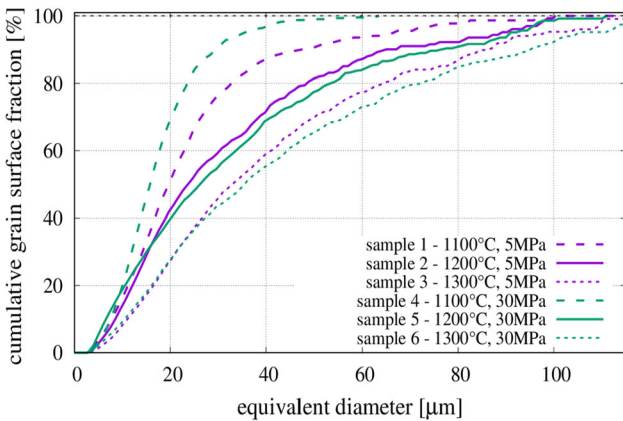


Fig. 8—Cumulative grain surface distribution as a function of grain size.

map of the grain size distribution of sample 1 (Figure 10(a)), where the lowest fraction with the blue colour dominates the map. It should be noted that in many cases, small grains are the part of single particle body of sintered powder which was denoted in the map of sample 1 by orange rings. The map of sample 3 (Figure 10(b)) indicates different microstructural features. On the one hand, the lowest fraction of the grain still constitutes a notable part, but on the other hand, the fractions with a diameter over 40 μm become much more identifiable with around 40 pct of the total grain area.

As stated earlier, the grain aggregates forming the powder particle (sample 1) were replaced by “single-oriented” large grains (sample 3), resulting in the grain growth. The scientific evidence of the lattice reorientation of grains, which can be defined as a process accompanying the densification of materials, typically occurring at the early stage of sintering<sup>[57]</sup> can be found in several works related to the sintering process. A similar behaviour can be observed in the case of materials subjected to long-term annealing at elevated temperatures<sup>[58]</sup> or materials exposed to cyclic thermal changes.<sup>[59]</sup> For example, as reported by Yeadon,<sup>[60]</sup> the adjustment of the crystallographic lattice orientation in the interface region was obtained during the sintering of copper powder directly on a copper substrate. The reorientation process was caused by a surface diffusion mechanism accompanying the neck formation and their growth and additionally by the migration of the grain boundary through the individual particles. The

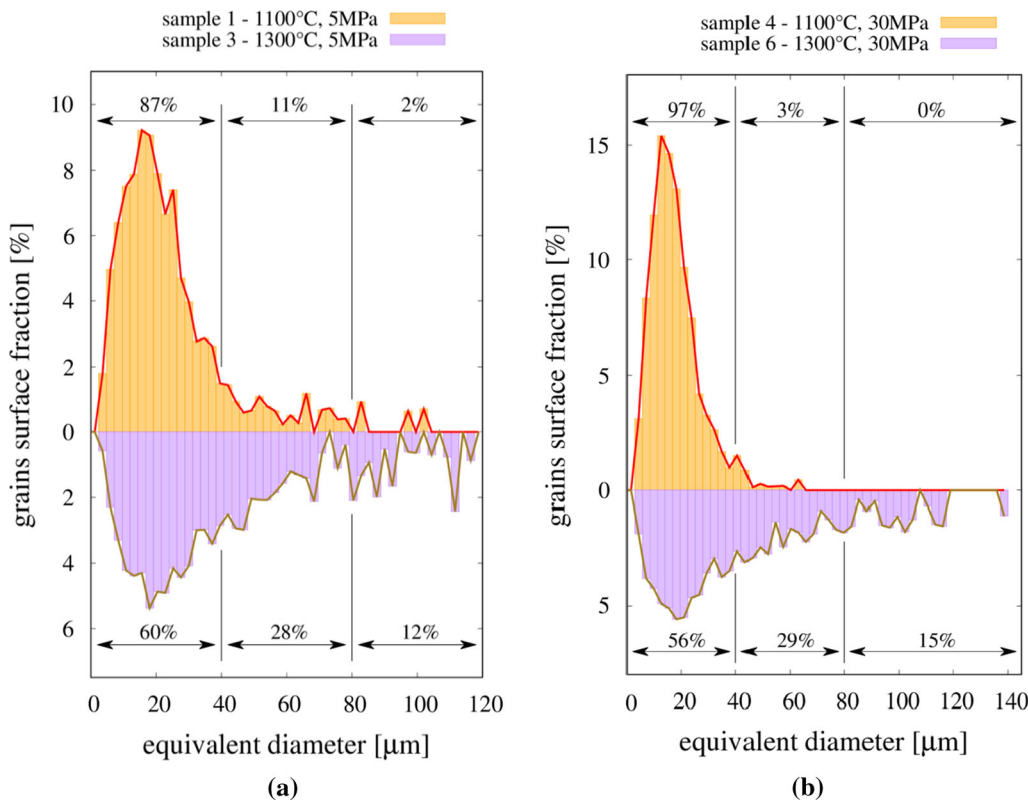
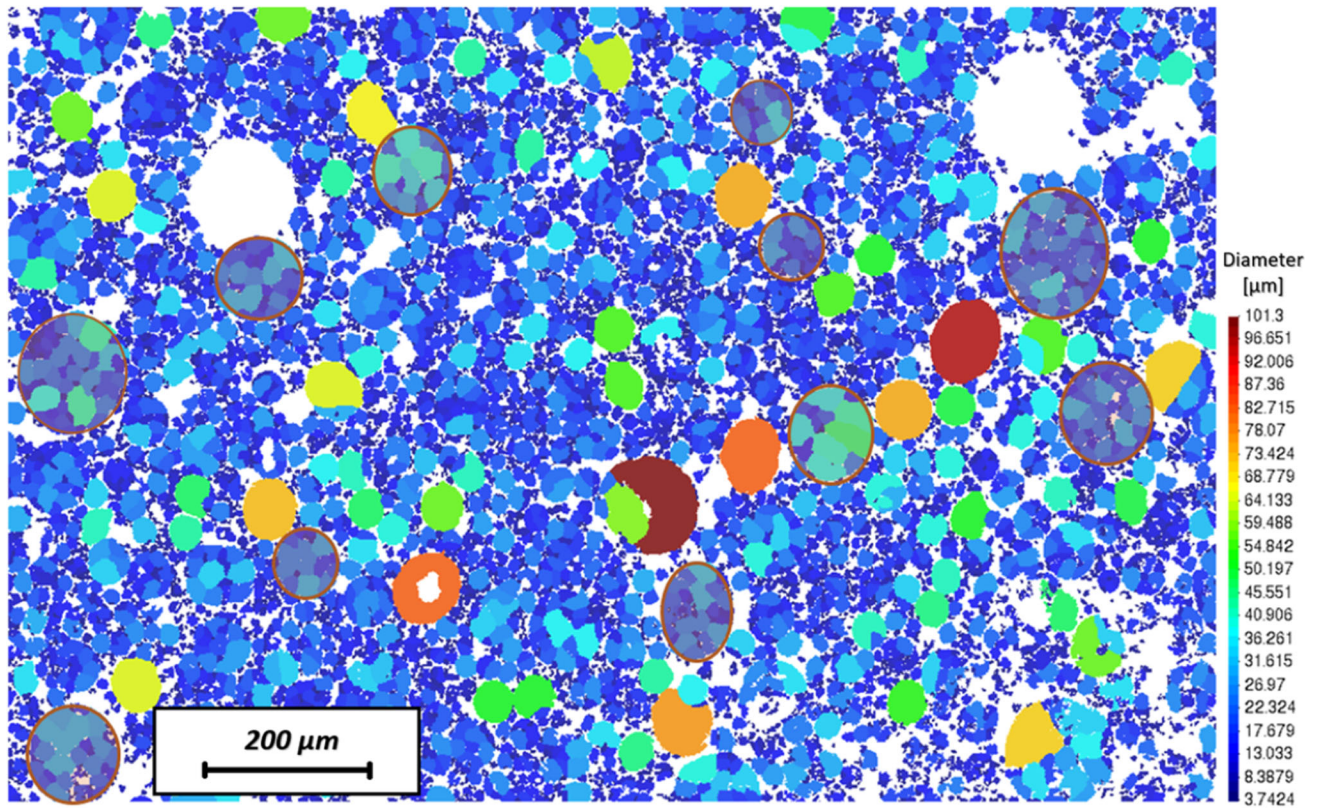
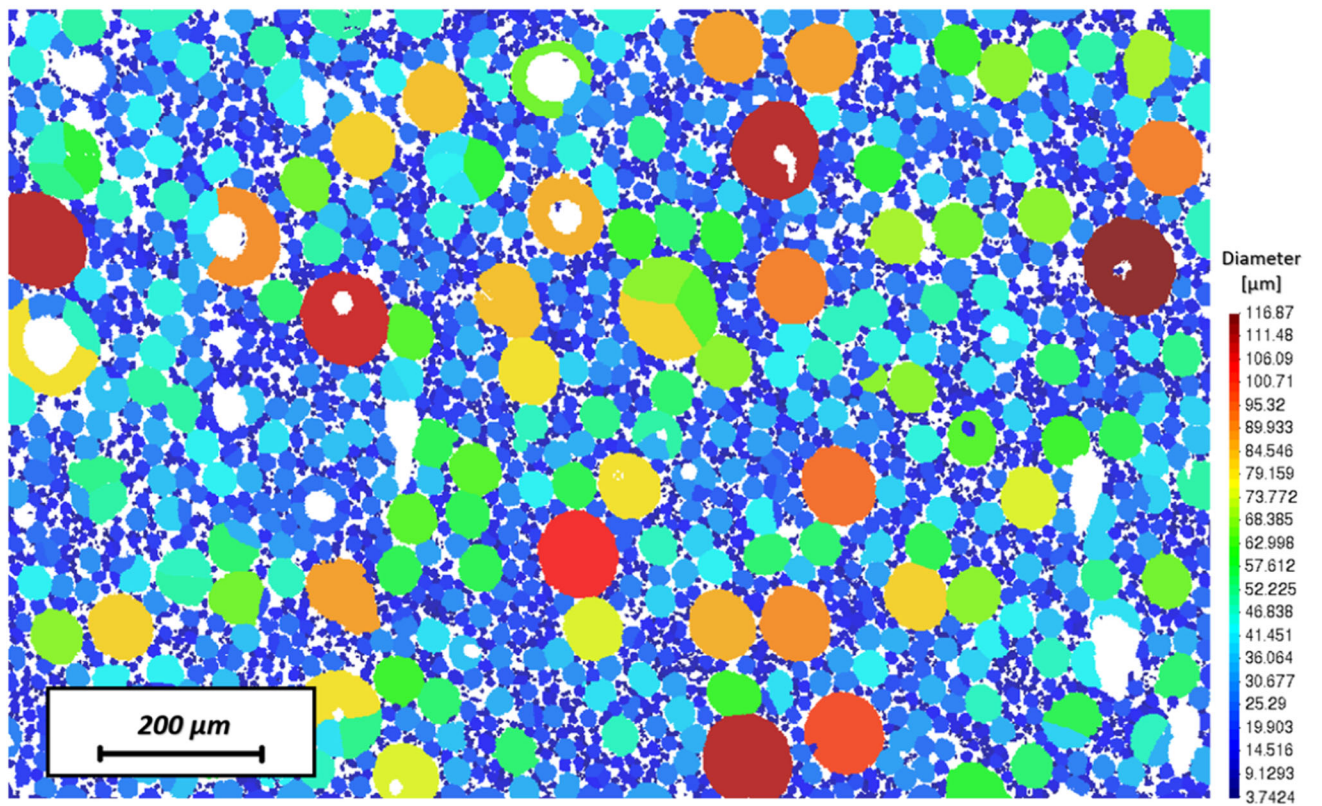


Fig. 9—Surface fraction distribution of the sample grain size sintered at: (a) 5 and (b) 30 MPa.



(a)



(b)

Fig. 10—Graphical representation of the grain size distribution of: (a) sample 1-(1100 °C/5 MPa) and (b) sample 3-(1300 °C/5 MPa) (Color figure online).

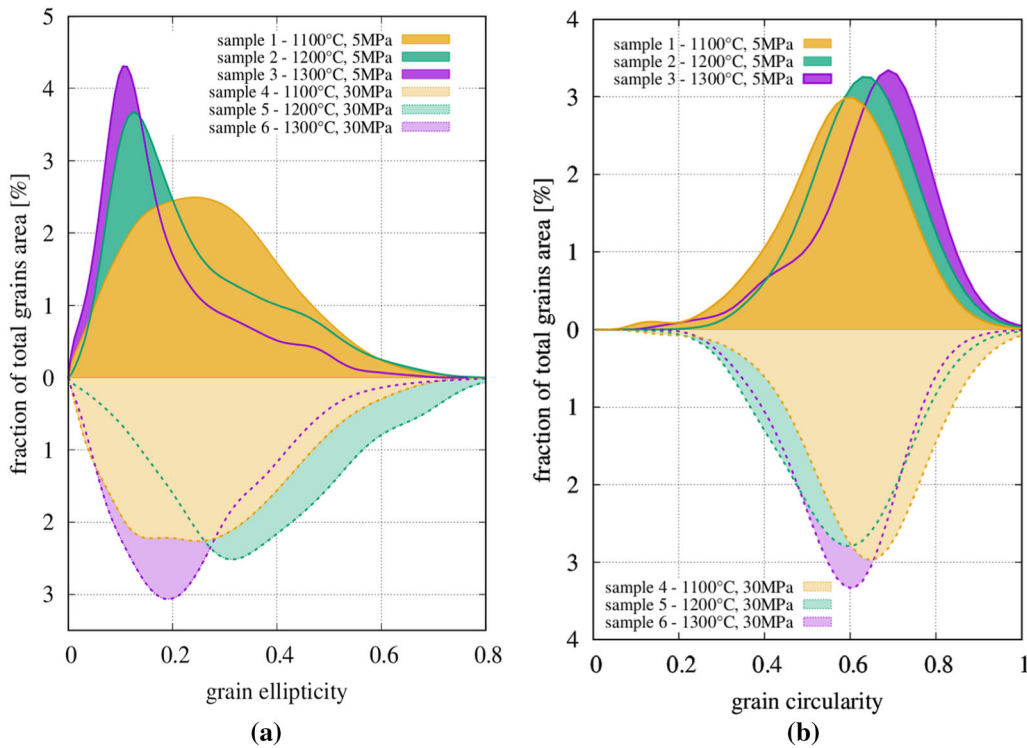


Fig. 11—The distribution of grain: (a) ellipticity and (b) circularity.

boundaries between the grains move to reduce the total grain boundary energy of the ensemble. Grupp *et al.*<sup>[61]</sup> postulated that except for the translation, rolling, and rotation of powder particles during sintering, the sliding of the grain boundary plays an important role in the reorientation process.

According to the research of Biswas,<sup>[62]</sup> the crystallographic orientation plays a critical role in the consolidation kinetics, as well as in the final microstructural configuration. In the case of materials densified *via* the SPS method, the directed current flow can also lead to grain reorientation, which was reflected in the grain growth and in the increase in the maximum grain size of the samples  $d_{\max}$  (Table I). The samples sintered at the sintering temperature of 1300 °C indicate the highest value of  $d_{\max}$ .

On the one hand, a decisive advantage of the SPS method resulting from the short process time is the possibility of sintering materials without significant grain growth, which has a fundamental importance for the manufacturing of nanomaterials.<sup>[55]</sup> On the other hand, grain growth cannot be entirely prevented, and the particles are dragged around by the migrating grain boundaries, coalescing in the process. Therefore, the typical final microstructures are characterized by rounded particles of equilibrium shape, often coarser than the original particles added as powder and predominantly situated at grain boundaries and (especially) triple lines. The mentioned shape effect is discussed in the next section.

#### D. Grain Shape

Beyond the influence on the grain size and homogenization of the microstructure, the increase in the sintering temperature and pressure leads to a considerable change in the grain shape. Its evolution has been demonstrated by the application of two parameters, grain ellipticity  $E$  and circularity  $C$ , by Eqs. [3] and [4], respectively. The distribution of the grain ellipticity and circularity for each sample is shown in Figure 11.

Considering the samples produced at lower applied pressures (upper side of Figure 11(a)), the temperature growth results in a decrease in the grain ellipticity, producing a narrower distribution with a higher maximum value. Simultaneously, the grain circularity of such samples (upper side of Figure 11(b)) approaches 1, indicating a less complex shape of grains with boundaries indicating a more rounded curvature. Such a shape effect is related to the driving force of the sintering process, forcing the system to obtain the lowest possible total energy.<sup>[57,63]</sup> The atoms and ions on the free surface have an excess energy compared to the identical structural elements inside the particle. In addition, a higher concentration of structural defects is observed in the subsurface layers than in its interior, and sometimes, it also applies to a different chemical composition of the material. The efforts of the system to reduce the surface energy are accompanied by changes in the shape of the sintered particles. The shape with the lowest energy is a sphere; therefore, along with the compaction of the material, rounding of the sintered grains is observed.<sup>[64,65]</sup>

The mentioned evolution of the grain shape can also be observed in the maps in Figures 10(a) and (b), which reveal the microstructural difference of samples 1 and 3 in the context of both grain size and shape. Such a relationship between the grain surface fraction, size, and shape is presented in the form of the 3D maps in Figure 12. The presented multi-parametric analysis provides the specific suggestion, which grain size fraction is mainly responsible for the change of grain shape. Comparing the two maps, it is clear that the small grains with a less circular shape (Figure 12(a)) have been replaced by larger ones with a more rounded shape. Moreover, this feature was confirmed by the weighted average value of the grain ellipticity  $E_{av}$  displayed in Table I. The global parameter, which combines the size and shape of grains, considerably decreases by 33 pct, proving the significant impact of the sintering temperature on the microstructure of the sample produced at a lower pressure.

In contrast with the 5 MPa samples, the investigation of the grain shape is more complex for the sample manufactured at a higher external pressure (30 MPa). In the 2D analysis, the grain shape should depend on the considered plane in relation to the applied pressure (see Figure 2). EBSD data of samples 4 and 6 were determined from the plane perpendicular to the application of the uniaxial pressure and electric current, while the data of sample 5 were determined from the parallel plane. The effect of the grain shape analysis from different planes of sintered samples can be seen in Figure 11, which shows a serious deviation of the grain ellipticity results of sample 5 to higher values, approaching unity. Such a deviation was also disclosed by means of the weighted average value of  $E_{av}$  (Table I), which increases by 57 pct for sample 5 compared to sample 6. The impact of the uniaxial pressure on the grain ellipticity of sample 5 is presented in Figures 13(a) and (b) in the form of a 3D map and microstructure representation, respectively.

The 3D map combining the percentage of total grain area, ellipticity, and diameter confirms the change in the grain shape of all fractions of grain size (up to 60  $\mu\text{m}$  and the largest one with a diameter of around 100  $\mu\text{m}$ ). Compared to the 3D map of sample 3 (high sintering temperature, low pressure), the difference is significant. Moreover, when investigating the maps of sample 5 (Figure 13(b)), sample 3 (Figure 10(b)), and sample 6 (Figure 7(b)), the variation in the grain shapes with a serious compaction effect of the grain structure of sample 5 can be seen. Due to the fact that the largest diameter of elliptical grains, in most cases, can be set along the horizontal direction of the image, we can assume that the direction of uniaxial pressure application is along the vertical axis. While relatively flattened and compressed grains are the characteristic geometrical features of sample 5, the uniaxial and rounded grains can be treated as a trademark of the structures sintered without high pressure (sample 3) and those obtained from the perpendicular plane to the pressure performance (sample 6).

The investigated plane of the sintered sample does not seem to affect the circularity of the grains. Hence, sample 5 does not deviate seriously from samples 4 and 6 (Figure 11(b)); however, they exhibit the reverse tendency compared to the samples sintered at 5 MPa. A higher sintering temperature supports the grain circularity in the case of lower pressure samples, but for the higher pressure samples, it is the opposite. The explanation of such an effect lies with the considerable increase in the structure densification and porosity elimination as powder particles approach each other at the microscopic scale which causes the structure shrinkage at the macroscopic scale.<sup>[40,54]</sup> As the process occurs, more grains seem to be in contact with the longer grain boundaries (please see Sections III-E and III-F). In order to fill the voids and pores within the structure and ensure the highest possible density, neighbouring grains tend to fit each other and match their shape at the contact zone. The shape adjustment deprives the grains of their circular shape with rounded curvatures. As a consequence, the grain shape becomes more polygonal with straight and linear edges.

### E. Contact Analysis

As confirmed in the previous subsections, the increase in the sintering temperature and pressure clearly impacts the geometrical features of the grains at the microscopic level. As a consequence, the evolution of the grain size and shape indicates the changes in the characteristics of the grain contacts. Thus, the investigation of the structure connectivity with an emphasis on the number of contacts/neighbours and the relationship to grain size was performed on the basis of the averaged quantities presented in Table I and the distributions of the microscopic parameters shown below.

The grain contact analysis is strictly related to the densification level (surface fraction), the grain number, and their sizes.<sup>[39]</sup> On the one hand, assuming the constant surface domain (such an image area), the density growth should promote the number of grains and consequently the number of contacts. As the sintering occurs, the sintering driving force and lower viscosity facilitate the powder grains approaching each other, causing new contacts with larger contact areas at the micro-level and, as a result, producing the material shrinkage at the macroscale.<sup>[66]</sup> On the other hand, grain growth occurring during the sintering process does the opposite and effectively reduces the grain and contact count at the expense of an increased single grain surface. A higher sintering temperature (from 1100 °C to 1300 °C) results in a larger grain size (see Section III-B) and, in turn, decreases the equivalent grain number (per specific area) and equivalent number of contacts within a given applied pressure by around 50 pct in both cases (Table I). Having the similar reduction rate of both parameters along with the temperature rise, the global coordination number has an approximately constant value for a certain pressure; thus, it is basically unaffected by the sintering temperature. This particular effect can also be seen in Figure 14(a), which shows the

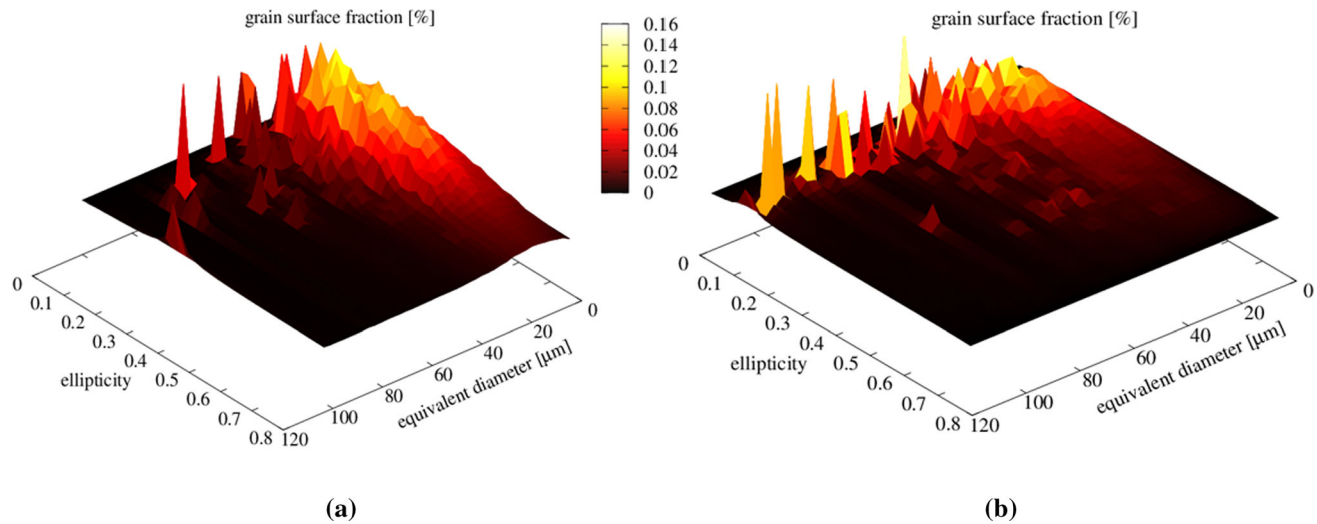


Fig. 12.—3D maps of the fraction of total grain area as a function of grain ellipticity and size of: (a) sample 1-(1100 °C/5 MPa) and (b) sample 3-(1300 °C/5 MPa).

comparable distributions of grain percentage as a function of the number of neighbours.

The images of the samples sintered at 5 MPa reveal over 2 pct of the grains without any neighbours. This issue can be explained by the specificity of the 2D analysis, which excludes the third dimension where possible contacts may occur.<sup>[43]</sup> Moreover, the low external pressure does not ensure the effective particle rearrangement, thereby limiting the starting number of contacts even before the spark plasma sintering.

According to the distribution in Figure 14, the grains of the “lower pressure samples” interact most frequently with three other grains regardless of the applied sintering temperature. Similarly, grains of the 30 MPa samples reveal a close tendency; however, the impact of a higher pressure on the grain contact properties seems to be crucial. The expected dependence of the higher number of equivalent grains (per specific area) and contact number of samples sintered at 30 MPa compared to 5 MPa in certain sintering temperatures can be observed (Table I). For all cases (1100 °C, 1200 °C, and 1300 °C), the growth of the equivalent grain number from 5 to 30 MPa is in the range of 30–50 pct. Simultaneously, the equivalent number of contacts grows by 90–100 pct and, therefore, increases the global coordination number (calculated *via* Eq. [6]) to values in the range of 9.4–10.4. Corresponding to this effect, Figure 14(b) presents the deviation of the grain count between samples sintered at 5 and 30 MPa as a function of the number of neighbours.

It is clear that the “lower pressure samples” contain more grains with the lowest number of neighbours (up to 2). As the sintering temperature is higher, the deviation of the grain number for the lowest range of contact numbers increases, and the lowest range itself is getting wider (from 0–2 at 1100 °C to 0–3 at 1300 °C). For neighbours range starting from 4, the samples sintered at 30 MPa indicate a much higher count of

grains and the difference increases as the temperature increases. Intuitively, the larger number of contacts seems to be associated with larger grains. Figures 15(a) and (b) confirm the relationship between grain contacts and grain size.

The first graph displays the average number of neighbours related to a certain equivalent grain diameter. The curves were approximated by a linear function, which seems to be a good representation regardless of the applied sintering pressure and temperature. It can be seen that the curves representing the samples sintered at 5 MPa basically coincide with each other and indicate a highly similar quantitative character. Moreover, as mentioned previously, the application of a higher external pressure during spark plasma sintering ensures the greater contact count for a certain grain size. As the grain diameter is larger, the difference in the average number of neighbours for various pressures increases.

Here, it can be seen that the serious deviation of the curve representing sample 5 makes this effect even larger. The issue is associated with the fact that the EBSD image was obtained from a different plane compared to the other samples. As discussed in Section III-C, the plane parallel to the direction of the pressure and electric current application reveals a relevant perspective of the material microstructure characterized by deformed and compressed grains subjected to a relatively high uniaxial loading (Figure 2). Along with a more complex shape of grains (Figures 11 and 13), such a microstructure ensures more contact counts for larger grains.

The investigation corresponding to Figure 15(a) answers a question of how many contacts on average is assigned to each grain size. The next graph in Figure 15(b) discloses the percentage of total count of grain-grain contacts as a function of grain diameter. It is clear that the smallest grain fraction is responsible for the most contacts in total. As the grain diameter



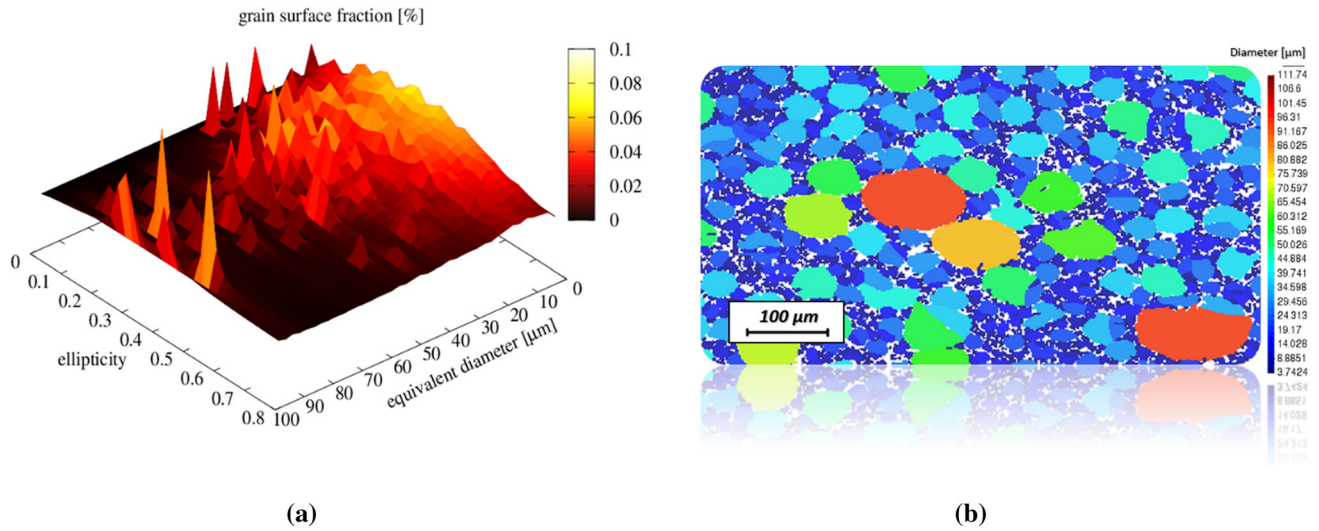


Fig. 13—3D map of the fraction of total grain area as a function of grain ellipticity and size (a) of sample 5-(1200 °C/30 MPa) with graphical representation of the sample structure (b).

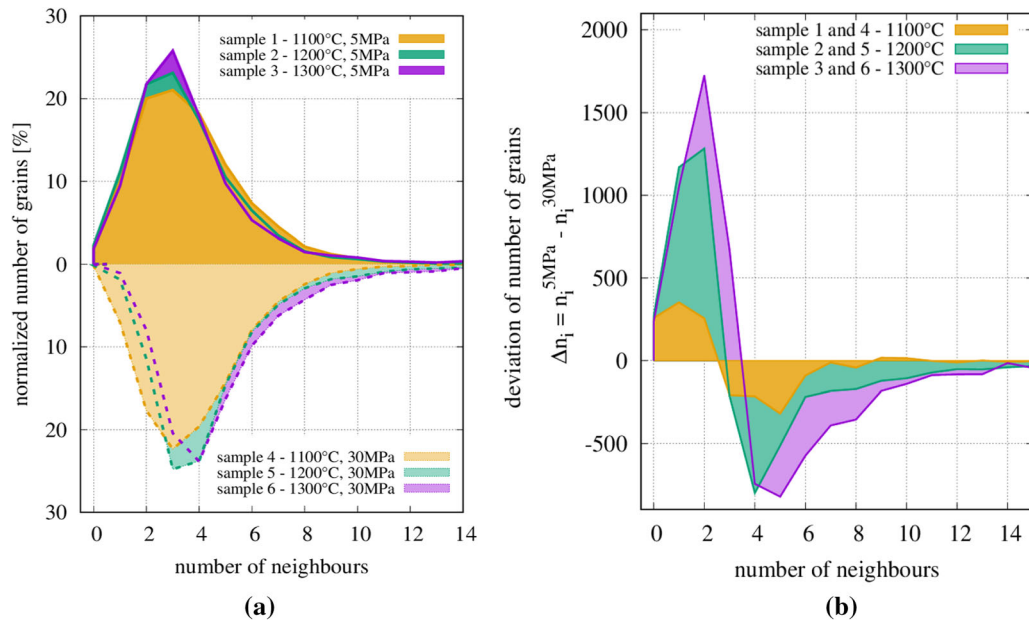


Fig. 14—The distribution of total grain percentage (a) and the deviation of the grain count between samples sintered at 5 and 30 MPa (b) as a function of the number of neighbours.

increases, a greater difference between the samples sintered at different temperatures can be observed mainly due to the grain growth phenomenon (Section III-B). Once again, it should be mentioned that the microstructure of sample 5 (different studied plane) deviates from the rest of the samples by the occurrence of more frequent contacts in the smallest size fraction (up to 10  $\mu\text{m}$ ) at the cost of a lower normalized contact count in the medium fraction (15–30  $\mu\text{m}$ ). The most probable explanation of this effect is related to the compaction stage before spark plasma sintering and the high mobility of the smallest particles through the spaces between the larger ones, which create the peculiar material skeleton limiting the movement of the larger

fraction. Due to their size, fine particles driven by a uniaxial applied loading easily fill the gaps and voids, thereby increasing the contact count. Generally, this effect should be observed in every plane of samples manufactured at higher pressures; however, it is manifested mostly in the perspective plane parallel to the direction of the force loading, as confirmed in sample 5.

Finally, the dependence of the grain contact number and grain size for each sintered sample can be seen in Table I by means of the weighted coordination number. On the one hand, similar to the standard one, the weighted global coordination number depends on the applied pressure (higher value for higher pressure). However, on the other hand, it increases along with the

sintering temperature, unlike the standard one. Here, the temperature-dependent grain growth drives the expansion of the parameter. It is manifested when comparing sample 3, which indicates a lower surface fraction (~ 84 pct) and much higher weighted coordination number than sample 4 with a surface fraction of ~ 91 pct. It is also worth noting the comparable values of the parameter for samples 5 and 6. In spite of the difference in the surface fraction, the microstructure of sample 5 tends to obtain a relatively high value of the weighted coordination number due to the privileged studied plane.

#### F. Grain Boundary Analysis

The investigation performed in the previous subsection provides a number of remarks showing the link between the spark plasma sintering parameters and the nature of the grain interactions. Now, let us study the magnitude of the grain contacts by means of two parameters—the grain boundary length of each grain contact  $l^{gb}$  and the grain boundary fraction of each grain  $f^{gb}$ , which were introduced in Section II–B.

First, as we can observe in Table I, the equivalent total grain boundary length of samples sintered at a certain pressure decreases as the sintering temperature increases. Moreover, the increase in the SPS pressure provides a much longer total GB in the studied representative surface. While the grain boundary length is a result of the grain number, the contact number, and grain size, its dependence on the sintering parameters will be similar to the other mentioned contact quantities (Table I—see contact section). By dividing the total grain boundary length by the equivalent grain number and introducing the average grain boundary length  $l_{av}^{gb}$ , we can notice a similar impact of the sintering parameters such as the global coordination number. The increase in the sintering temperature from 1100 °C to 1200 °C associated with the grain growth causes the drop in the average grain boundary length; however, the additional temperature increase (to 1300 °C) provides a higher value of the parameter irrespective of the applied pressure.

The temperature effect described by the average parameter and analysed from the macroscopic perspective has its source in every local contact of the bonding grains. It can be observed in Figure 16, where the cumulative and normal distribution (as a thumbnail figure) of the total contact number with respect to the grain boundary length is presented. Considering both distributions, an interesting remark can be made by studying the samples sintered at the same temperature and different pressures. In every case, the samples with the higher pressure reveals the higher amount of the smallest bonds, as a percentage, with respect to those with the lower pressure; however, for longer GB lengths, the relationship becomes reversed. The explanation of this feature can be provided by studying the second local parameter—the grain boundary fraction.

In particular, when investigating the sintered structure using the grain boundary fraction  $f^{gb}$ , it allows us to

evaluate the occupancy degree of the boundary of each grain in accordance with the sintering temperature, pressure, and surface fraction. For this reason, the representative microstructures of the sintered samples with the graphical distribution of the grain boundary fraction were prepared (Figure 17). In order to supplement the analysis, the distribution of the total grain surface fraction as a function of the grain boundary fraction of each grain is presented in Figure 18.

Generally, as seen in Table I, the average grain boundary fraction  $f_{av}^{gb}$  increases along with the surface fraction of the samples with one exception. Sample 2 (1200 °C, 5 MPa) indicates a lower value of the parameter compared to sample 1 (1100 °C, 5 MPa). When we study Figure 17 with the microstructure maps, the reason for this fact is obvious.

The relatively high number of small grains located inside the powder particles demonstrates the highly developed contact zones (boundaries) with other “interparticle” grains. A greater fraction of its boundary is occupied by neighbours as the grain gets redder in colour. Such grains can be found mostly in samples 1 and 4, *i.e.*, those sintered at a lower temperature without a considerable effect of the grain reorientation, thus it overstates the results of grain boundary fraction. Moreover, such samples indicate a much wider distribution of  $f^{gb}$  with respect to those sintered at a higher temperature (Figure 18). It is worth emphasizing that the samples sintered at 1100 °C contain a relatively high number of grains with both zero and a full occupancy level of grain boundaries. The issue with the zero grain boundary fraction can be explained analogously to grains with zero neighbours (see Section III–E).

As the sintering temperature increases, the structure of the samples is becoming more homogeneous with a narrower  $f^{gb}$  distribution and a higher peak, which is basically moving to higher values of the parameter (especially for 30 MPa samples). It can be surprising that the  $f_{av}^{gb}$  value of the densest samples (Table I) resulting from  $f^{gb}$  of each grain (displayed as the distribution in Figure 18) is around 60–70 pct because their global surface fraction  $\rho$  is around 90–97 pct. The reason for such an effect may lie in the occurrence of the micro porosity exhibited in the form of the considerable number of small voids located in the grain boundaries (Figure 7(b)). The effect can also be enhanced with the pixel size (1  $\mu\text{m}$ ) referenced to the grain size. Most likely, the decrease in the pixel size should increase the accuracy of the EBSD mapping, revealing more details of the sample microstructures and their features, such as the shape complexity of the grain boundaries and micropores.

#### G. Heat Conduction Simulations

EBSB-based finite element simulations were performed by the methodology presented in Section II–C. The simulations of heat transfer were carried out for six maps related to six NiAl sintered samples. The graphical distributions of the heat flux magnitudes  $q$  representative of the most porous structure (sample 2 with

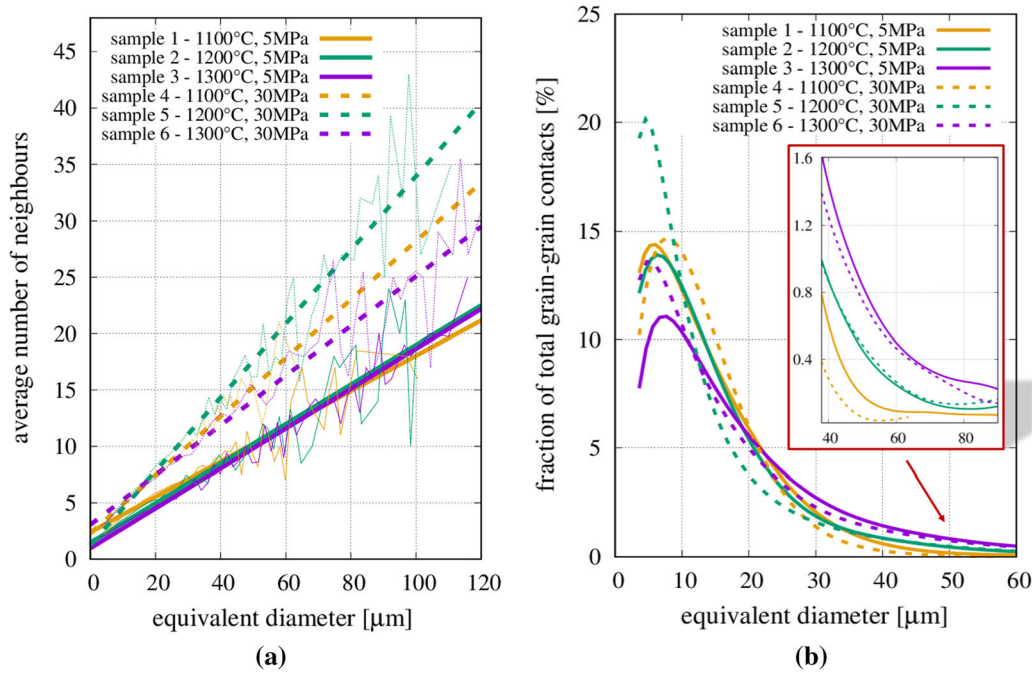


Fig. 15—The average number of neighbors (a) and percentage of total count of grain-grain contacts (b) as a function of grain diameter.

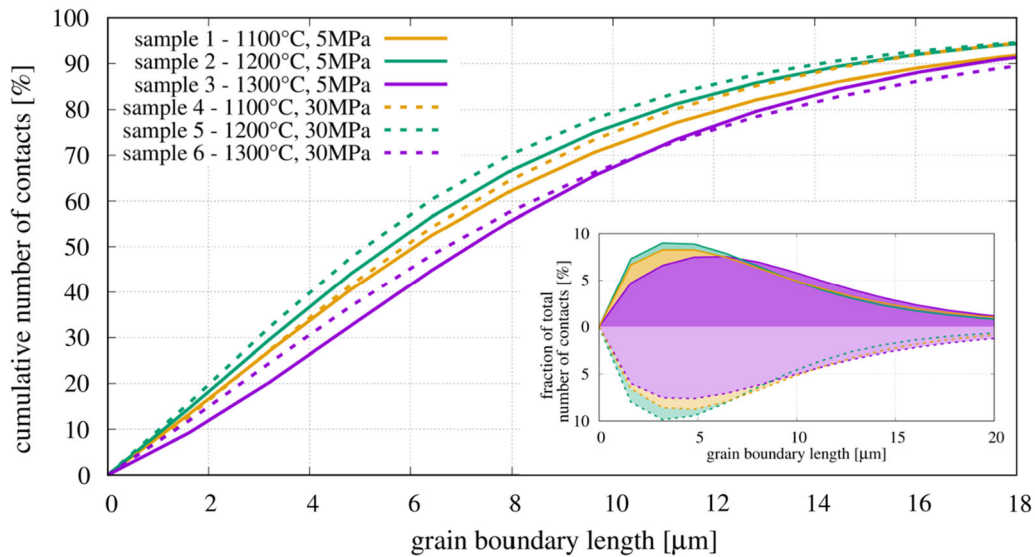


Fig. 16—Cumulative and normal distribution of the contacts count as a function of the grain boundary length  $l^{gb}$ .

$d_{rel} = 78.8$  pct) and the most dense one (sample 6 with  $d_{rel} = 96.7$  pct) are shown in Figures 19(a) and (b), respectively. The scale of the magnitudes of  $q$  was set uniformly for both figures to allow for the comparison of the values on both structures. Regardless of the map porosity, we can distinguish several features related to the structural characteristic. The finite elements assigned to the porosity/voids due to the nearly zero value of the thermal conductivity indicate low  $q$  values (blue colour). Similarly, the isolated grains with either no or limited bondings with other grains in the perpendicular direction of the heat flow axis exhibit minor heat flux

magnitudes. Such a thermal effect can be observed mostly in the case of most porous samples, sintered in 5 MPa, showing the reduced number of contacts (see Section III-E) and grain boundary fraction of grains (see Section III-F).

Due to the advantageous sintering conditions affecting low porosity and significantly higher connectivity of grains, the mentioned effect is considerable less noticeable in the case of samples 4–6 manufactured at 30 MPa of external pressure. Here, the dominant thermal features is the flow through the grain body (green colour—Figure 19(b)). A relatively high thermal conductivity of

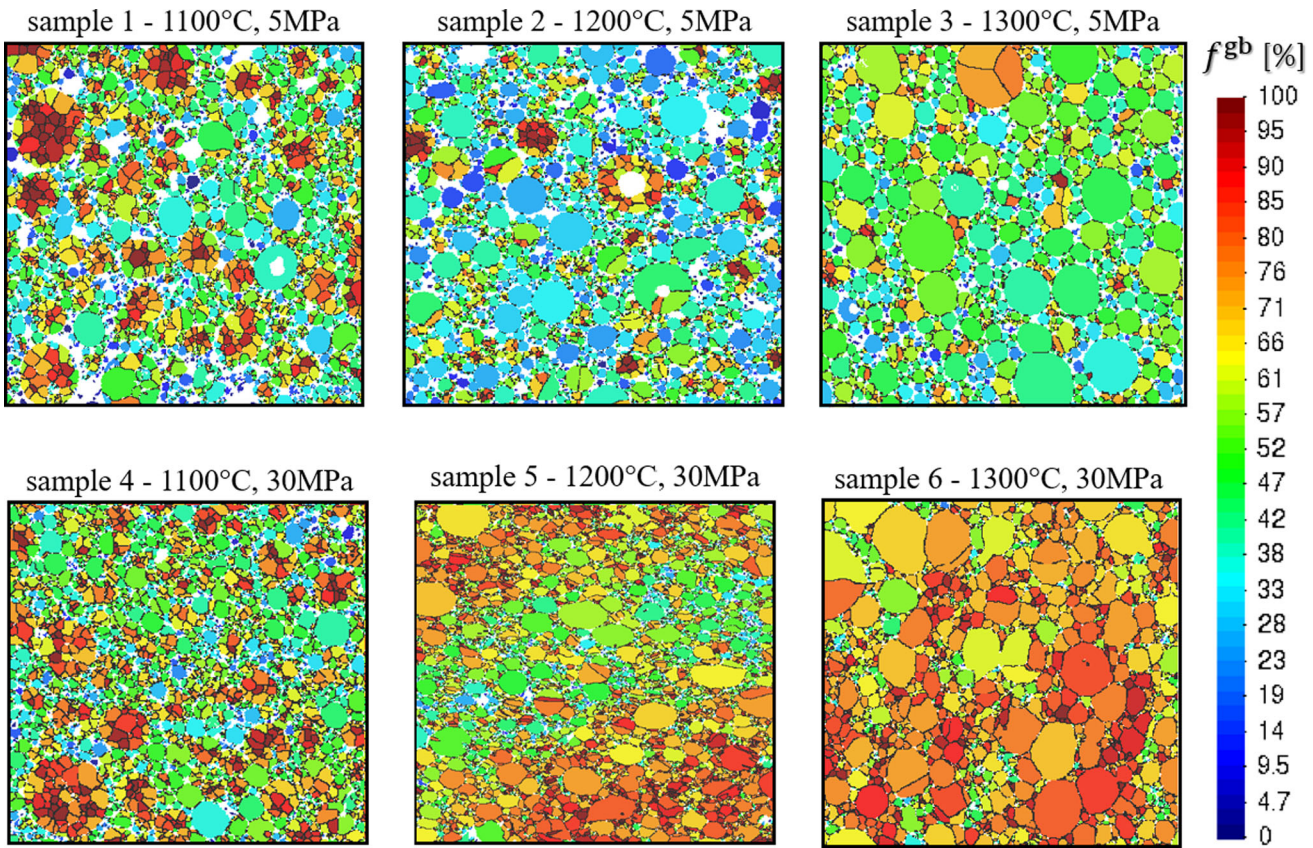


Fig. 17—Representative sample microstructures with the graphical distribution of the grain boundary fraction  $f^{gb}$ .

the finite element assigned to the grains accompanied by the low number of structural constrictions in the form of necks ensure the homogeneous heat flow through the whole sample. It is clearly reflected in the distributions of the magnitude of local heat fluxes  $q$  and deviation angles from the prescribed direction of the heat flux  $\beta$  presented in Figures 20(a) and (b), respectively. The first one shows the relatively narrow peak indicating the high magnitudes of element heat flux  $q$  for the most dense samples. The second one, illustrating the deviation angles, displayed the slight directional variation of the heat flux vectors, which is confirmed by the average values of  $q_{av}$  and  $\beta_{av}$  presented in Table I.

A completely different behaviour can be seen in the case of samples 1–3 manufactured in lower external pressure. The larger number of pores and voids forced to deflect the heat fluxes from the prescribed direction of flow as they approached the physical obstacles, *i.e.*, pores.<sup>[10]</sup> Furthermore, the distribution of  $q$  of the less-dense samples can be characterized by a heterogeneous and wide-spread range with a quite large standard deviation (Table I). As noticed previously and confirmed in Figure 11, the lowest  $q$  values of samples 1–3 are associated with the limited connectivity of grains; thus, substantial peaks for those samples close to the zero value of  $q$  (Figure 20(a)) can be seen.

In turn, the maximum element heat fluxes (red/grey colour in Figure 19(a)) are located at the bottle-shaped necks between the particles constituting the

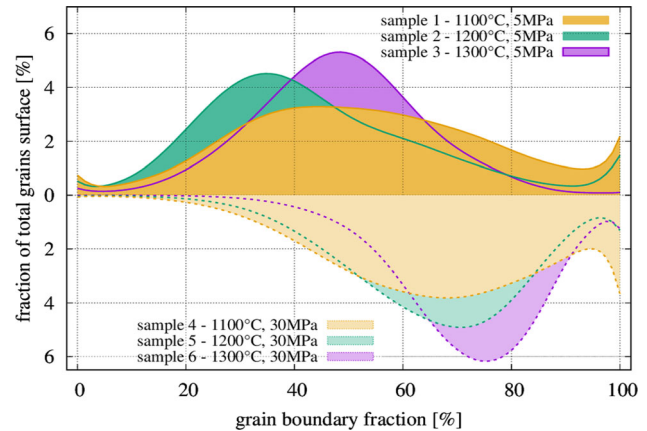
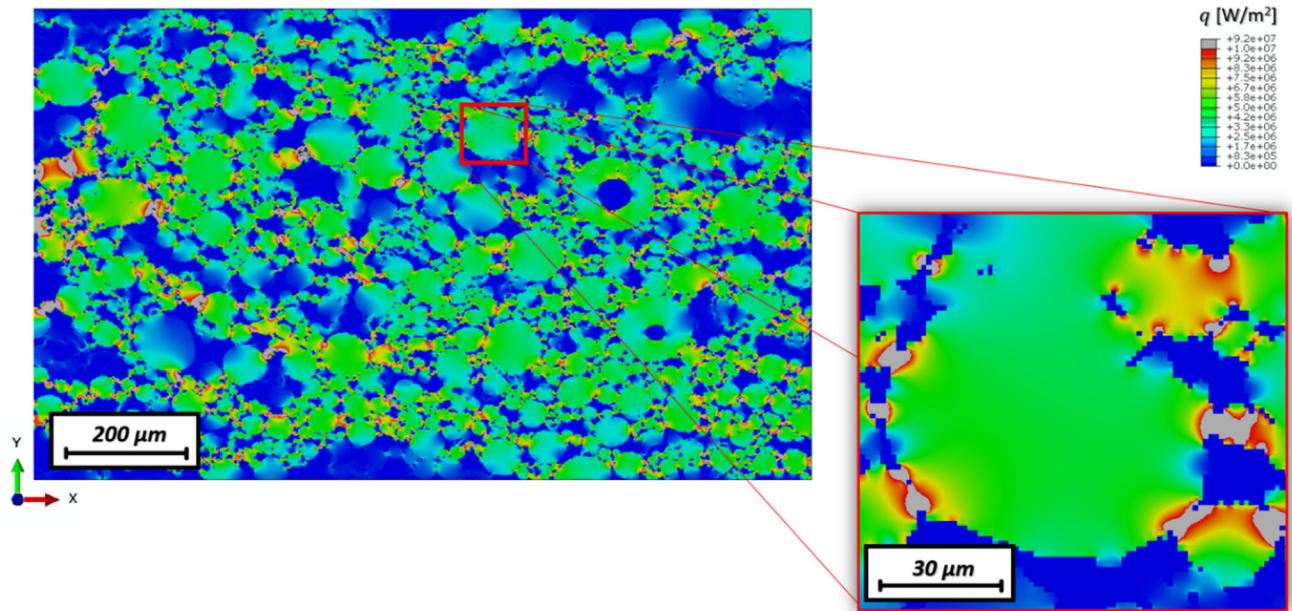
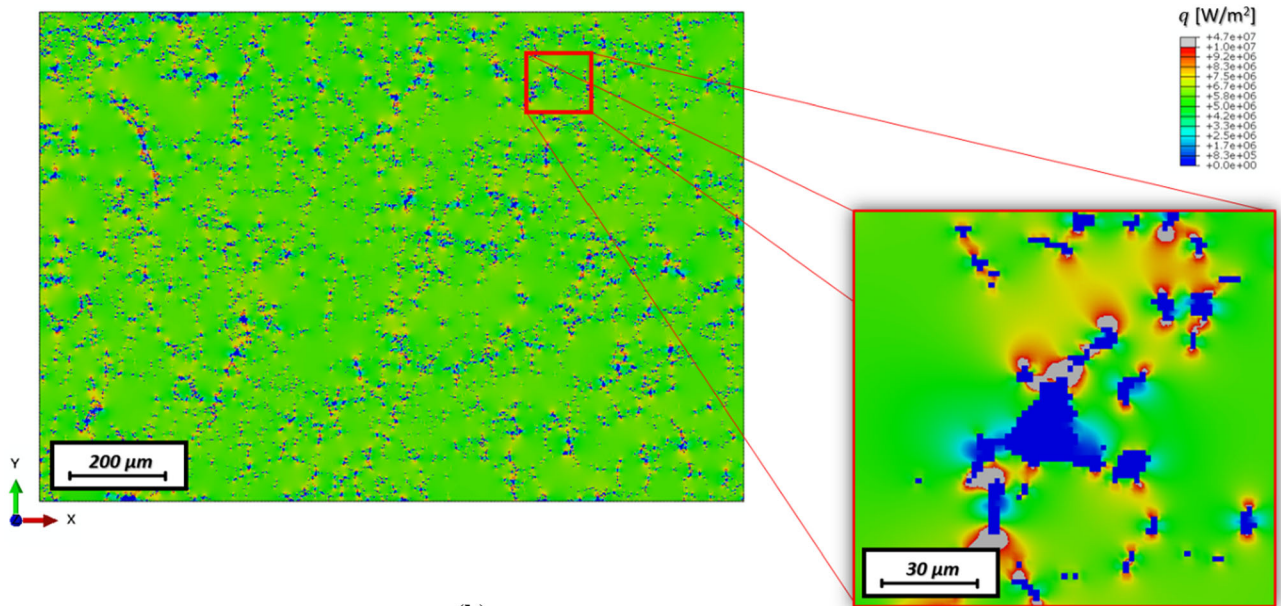


Fig. 18—The distribution of the grain surface fraction as a function of the grain boundary fraction.

reduced-sized channels for heat conduction. In contrast to micro-CT based FEM,<sup>[33]</sup> EBSD-based FEM allows the finite element results related to both the grain boundary and grain interior to be distinguished. Taking advantage of such a feature, the ratio of the average values of the heat fluxes of the elements corresponding to the grain boundaries and grain interior,  $q_{av}^{gb}/q_{av}^{gr}$ , is introduced and presented in Table I. It can be confirmed that samples 1–3 indicate a much higher ratio than samples 4–6 due to the lower number of contacts, lower



(a)



(b)

Fig. 19—Graphical distribution of the heat flux magnitudes  $q$  in: (a) sample 2 ( $d_{\text{rel}} = 78.8$  pct) and (b) sample 6 ( $d_{\text{rel}} = 96.7$  pct) (Color figure online).

grain boundary length  $l^{\text{gb}}$ , and lower grain boundary fraction  $f^{\text{gb}}$ , which together support the concentration of heat fluxes on the grain boundaries. An interesting issue is related to the fact that sample 1 exhibits a lower  $q_{\text{av}}^{\text{gb}}/q_{\text{av}}^{\text{gr}}$  ratio than samples 2 and 3. Because sample 1 reveals the clusters of small grains creating the single particle

body, their grain boundaries (connections between grains), in contrast to particle boundaries (necks), do not constitute the serious hinder as heat flows. Finally, as the density of the maps increased, the  $q_{\text{av}}^{\text{gb}}/q_{\text{av}}^{\text{gr}}$  ratio of the samples manufactured at 30 MPa decreases towards 1, indicating the location of high heat fluxes either at

grain boundaries, pore-grain interfaces, and the grain interior (Figure 19(b)).

All of the investigated local structural characteristics combined with the presented thermal one can be summarized by the single parameter treated as a macroscopic response of the porous microstructure. The effective thermal conductivity,  $\lambda_{\text{eff}}^{2\text{D}}$ , introduced by Eq. [8] in Section II-C was used to describe the structure connectivity. As opposed to the surface fraction showing the quantitative content of the solid phase,  $\lambda_{\text{eff}}^{2\text{D}}$  should be considered as a supplementary tool to assess the microstructural condition. However, it should not be considered as a real physical parameter related to the thermal properties because we study the two-dimensional case which generally excludes the comparison with experimental data.<sup>[44]</sup>

Figure 21 presents the summary of the effective thermal conductivity obtained from EBSD maps as a function of the relative density. The results display the linear dependence of  $\lambda_{\text{eff}}^{2\text{D}}$  and  $d_{\text{rel}}$ , which qualitatively agrees with most popular theoretical models (Maxwell-Eucken, Landauer)<sup>[46,51]</sup> and numerical FEM results<sup>[10]</sup> related to the thermal conductivity of porous materials.

Furthermore, to compare the 2D and 3D cases, we took advantage of the results of the effective thermal conductivity from micro-CT based FEM simulations of NiAl samples.<sup>[10]</sup> A considerable increase in the deviation between the EBSD-based and micro-CT based FEM results can be observed as the density grows. A relatively large reduction of  $\lambda_{\text{eff}}^{2\text{D}}$  with the increase in the porosity has an analogous tendency as in Reference 43. Certainly, such an effect is closely associated with discrepancies between the two-dimensional and three-dimensional structure representation. Less degrees of freedom of the heat flux and the separation of individual grains lead to the significant reduction of  $\lambda_{\text{eff}}^{2\text{D}}$ . As

presented in Section III-E, grains with zero neighbours most likely are in contact with other particles/grains, creating the continuous framework in the 3D microstructure. Fully separated grains and those with limited contact numbers in 2D do not transfer the heat flow effectively, which in 3D they served as extra pathways.<sup>[42]</sup> Moreover, a graphical distribution of grains of the most porous maps (Figure 10) proved the occurrence of several areas with the agglomeration of small unbonded grains, indicating a lower  $q$  and acting as heat blocking porous regions.<sup>[43]</sup> An insightful discussion of 2D and 3D thermal conductivity was performed in Reference 45.

The dependence between  $\lambda_{\text{eff}}^{2\text{D}}$  and  $\lambda_{\text{eff}}^{3\text{D}}$  of NiAl samples can be depicted by the following simple relation:

$$\lambda_{\text{eff}}^{2\text{D}} = \lambda_{\text{eff}}^{3\text{D}} - \Delta\lambda_{\text{eff}}(d_{\text{rel}}), \quad [11]$$

where  $\Delta\lambda_{\text{eff}}(d_{\text{rel}})$  denotes the correction/gap between  $\lambda_{\text{eff}}^{2\text{D}}$  and  $\lambda_{\text{eff}}^{3\text{D}}$  as a function of the relative density. Because the evolution of the gap shows a linear character, it can be predicted by a linear function with constant parameters  $a$  and  $b$ :

$$\Delta\lambda_{\text{eff}}(d_{\text{rel}}) = a \cdot d_{\text{rel}} + b. \quad [12]$$

As presented in Figure 21, the results of  $\lambda_{\text{eff}}^{3\text{D}}$  of NiAl samples obtained by micro-CT analysis were predicted by the analytical Landauer model using its reduced version (Eq. [10]). The theoretical results correspond well with FEM one as the relative density changes.<sup>[10]</sup> Based on this fact, we can express the analytical prediction of  $\lambda_{\text{eff}}^{2\text{D}}$  determined from the EBSD-based FEM results by the 2D correction to the Landauer model. By combining Eq. [11] with the 3D reduced version of the model (Eq. [10]) and the linear correction (Eq. [12]), we obtain:

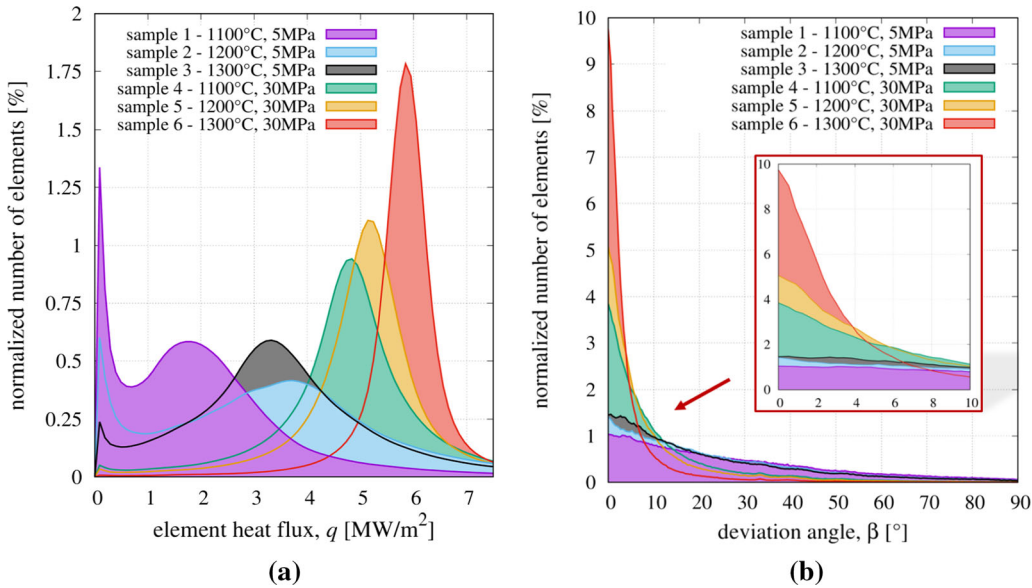


Fig. 20—The distributions of: (a) element heat fluxes (magnitude)  $q$  and (b) deviation angles from the prescribed direction of the heat flux (the central axis of flow)  $\beta$ .

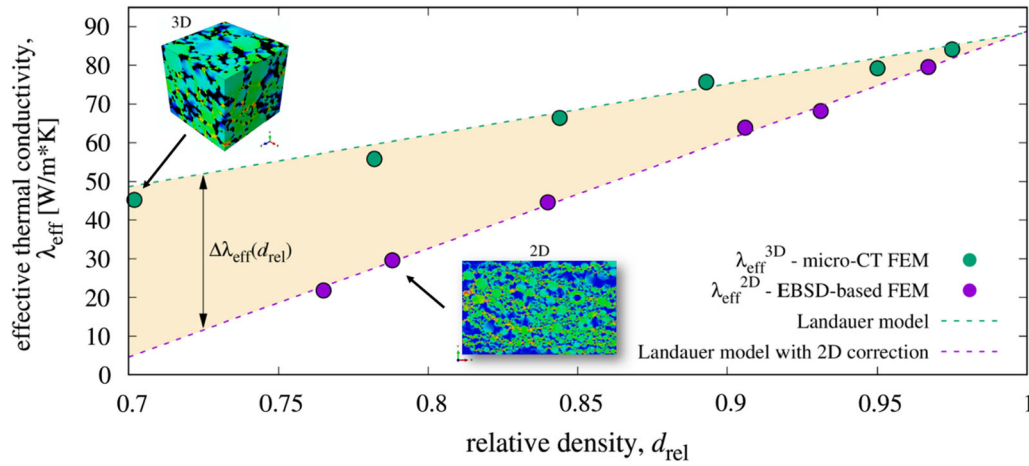


Fig. 21—Summary of the effective thermal conductivity obtained from EBSD maps (2D), micro-CT (3D) analysis,<sup>[10]</sup> and the prediction by the Landauer model and its 2D version.

$$\lambda_{\text{eff}}^{2\text{D}} = d_{\text{rel}}(1.5\lambda_s - a) - 0.5\lambda_s - b. \quad [13]$$

For the presented case of NiAl samples, the constant parameters are as follows:  $a = -148$ ,  $b = 147.7$ . Because the constant parameters indicate a close dependence, we can state that  $a \approx -b$ . The output of the proposed 2D Landauer model is presented in Figure 21, showing a desirable coincidence of the theoretical and numerical results.

#### IV. SUMMARY AND REMARKS

The presented work can be summarised in the following remarks:

- 1) Electron backscatter diffraction was employed to obtain the actual representation of the microstructure of the samples the nickel aluminide samples manufactured by spark plasma sintering. EBSD data were transferred to computer software for the quantitative analysis of the grain morphology to expose its dependence on process parameters.
- 2) The investigation of the homogeneity of the maps was performed by applying the concept of the representative and local surface element. The first one allows us to point the proper size of the EBSD data representations indicating a much lower one for samples manufactured in 30 MPa. The second one reveals high deviations of local homogeneity of samples which decreases as the porosity reduces.
- 3) The grain size study revealed the decisive impact of the sintering temperature on the lattice reorientation within the single powder particle and the resulting grain growth from approx. 10  $\mu\text{m}$  for samples manufactured at 1100  $^{\circ}\text{C}$  to approx. 12–13  $\mu\text{m}$  for those manufactured at 1300  $^{\circ}\text{C}$ .
- 4) EBSD grains representation proved the influence of the sintering process parameters on the grain

shape. The ellipticity of the grains grows as the sintering temperature and density increases regardless of the applied pressure. Similarly, the circularity of the grains also increased with more privileged sintering conditions; however, at higher density levels (over 90 pct), the reversal in the trend resulted in grains that were less circular with more complex boundaries adjusted to close neighbours.

- 5) The analysis of the grain contact and boundaries reveals the impact of two opposing sintering effects related to temperature. Regardless of the high impact of the external pressure, the first effect refers to the grain reorientation and their growth, which decreases the neighbour count and grain boundary length. The second, driven by the sintering process resulting in the increase in the sample densification, leads to the increase in the number of grain contacts and, thus, the grain boundary length and fraction.
- 6) All of the evaluated microstructural features significantly affect the connectivity of the studied EBSD maps reflected within the numerical simulations of heat conductions *via* the finite element framework. The effective thermal conductivity, introduced as the macroscopic response of the sample, decreases as the porosity grows. Such effect has its source in the thermal results calculated at the level of single grains, *i.e.*, the heat flux magnitude (the highest value for the densest samples) or deviation angle (the lowest value for the densest samples).
- 7) The EBSD-based FEM results of the effective thermal conductivity were confronted with the micro-CT FEM, showing the major quantitative difference stemming from the dimensional issue. Based on the 3D results, the special correction to the 2D case was introduced by the use of the analytical Landauer model, ensuring the required coincidence between the theoretical and numerical results.

## ACKNOWLEDGMENTS

The authors would like to acknowledge the financial support of the National Science Centre (DEC-2019/35/B/ST8/03158).

## CONFLICT OF INTEREST

On behalf of all authors, the corresponding author states that there is no conflict of interest.

## OPEN ACCESS

This article is licensed under a Creative Commons Attribution 4.0 International License, which permits use, sharing, adaptation, distribution and reproduction in any medium or format, as long as you give appropriate credit to the original author(s) and the source, provide a link to the Creative Commons licence, and indicate if changes were made. The images or other third party material in this article are included in the article's Creative Commons licence, unless indicated otherwise in a credit line to the material. If material is not included in the article's Creative Commons licence and your intended use is not permitted by statutory regulation or exceeds the permitted use, you will need to obtain permission directly from the copyright holder. To view a copy of this licence, visit <http://creativecommons.org/licenses/by/4.0/>.

## REFERENCES

1. R.M. German: *Sintering – Theory and Practice*, A Wiley Inter-science Publications, New York, 1996.
2. X. Boulnat, C. Lafont, J.B. Coudert, and C. Dayot: *Metall. Mater. Trans. A*, 2020, vol. 51, pp. 5318–27.
3. D. Zheng: *Metall. Mater. Trans. A*, 2022, vol. 53, pp. 2724–29.
4. B.K. Samantaray, S.R. Bakshi, K.V. Rajulapati, and S. Gollapudi: *Metall. Mater. Trans. A*, 2022, vol. 53, pp. 2680–88.
5. R. Orrù, R. Licheri, A.M. Locci, A. Cincotti, and G. Cao: *Mater. Sci. Eng.*, 2009, vol. 63(4–6), pp. 127–287.
6. P. Cavaliere, B. Sadeghi, and A. Shabani: *Spark Plasma Sintering: Process: Fundamentals*, in book *Spark Plasma Sintering of Materials Advances in Processing and Applications*, 2019, pp. 3–20.
7. J. Trapp and B. Kieback: *Powder Metall.*, 2019, vol. 62, pp. 297–306.
8. N. Sharma, S.N. Alam, and B.C. Ray: *Fundamentals of Spark Plasma Sintering (SPS): An Ideal Processing Technique for Fabrication of Metal Matrix Nanocomposites*, in book *Spark Plasma Sintering of Materials Advances in Processing and Applications*, 2019, pp. 21–59.
9. X. Li, Z. Liu, S. Cui, C. Luo, C. Li, and Z. Zhuang: *Comput. Methods Appl. Mech. Eng.*, 2019, vol. 347, pp. 735–53.
10. S. Nosewicz, G. Jurczak, T. Wejrzanowski, S. Ibrahim, A. Grabias, W. Węglewski, K. Kaszyca, J. Rojek, and M. Chmielewski: *Int. J. Heat Mass Transf.*, 2022, vol. 194, pp. 123070–1–119.
11. S. Nosewicz, J. Rojek, K. Wawrzyk, P. Kowalczyk, G. Maciejewski, and M. Maździarz: *Comput. Mater. Sci.*, 2019, vol. 156, pp. 385–95.
12. J. Zhang and A. Zavaliangos: *J. Electron. Mater.*, 2011, vol. 40, pp. 873–79.
13. A.J. Wilkinson and T.B. Britton: *Mater.*, 2012, vol. 15(9), pp. 366–76.
14. A.D. Rollett and K. Barmak: *Orientation Mapping*, in: *Physical Metallurgy (Fifth Edition)*, Elsevier B.V. 2014, pp. 1113–41.
15. P. Bobrowski, M. Faryna, and Z. Pędzich: *Mater. Res. Bull.*, 2014, vol. 57, pp. 203–09.
16. S.I. Wright and M.M. Nowell: *Microsc. Microanal.*, 2006, vol. 12, pp. 72–84.
17. L. Helmick, S. Dillon, K. Gerdes, R. Gemmen, G. Rohrer, S. Seetharaman, and P. Salvador: *Intl. J. Appl. Ceram. Technol.*, 2011, vol. 8, pp. 1218–28.
18. H. Beladi and G. Rohrer: *Acta Mater.*, 2013, vol. 61, pp. 1404–12.
19. A. Wojteczko, R. Lach, K. Wojteczko, and Z. Pędzich: *Ceram. Int.*, 2016, vol. 42, pp. 9438–42.
20. P. Bobrowski, M. Faryna, and Z. Pędzich: *J. Mater. Eng. Perform.*, 2017, vol. 26, pp. 4681–88.
21. I. Matuła, G. Dercz, M. Zubko, J. Maszybrocka, J. Jurek-Suliga, S. Golba, and I. Jendrzewska: *Materials*, 2020, vol. 13, p. 4539.
22. H. Liang, Y. Zeng, K. Zuo, Y. Xia, D. Yao, and J. Yin: *Ceram. Int.*, 2016, vol. 42, pp. 15679–86.
23. C. Machio, M.N. Mathabathe, and A.S. Bolokang: *J. Alloys Compd*, 2020, vol. 848, 156494.
24. Z. Xia, B. Chen, and K. Lu: *J. Mater. Sci.*, 2013, vol. 48, pp. 5852–61.
25. P. Bobrowski, Z. Pędzich, and M. Faryna: *Micron*, 2015, vol. 78, pp. 73–78.
26. T. Wejrzanowski, M. Lewandowska, and K.J. Kurzydłowski: *Image Anal. Stereol.*, 2010, vol. 29, pp. 1–2.
27. T. Ilzig, D. Schumacher, M. Wilhelm, S. Günther, and S. Odenbach: *Mater. Charact.*, 2021, vol. 174, 110966.
28. J. Fu, H.R. Thomas, and C. Li: *Earth-Sci. Rev.*, 2021, vol. 212, 103439.
29. Í. Carneiro and S. Simões: *Metals*, 2020, vol. 10, p. 1097.
30. T. Martinez Ostormujof, R.R.P. Purushottam Raj Purohit, S. Breumier, N. Gey, M. Salib, and L. Germain: *Mater. Charact.*, 2022, vol. 184, pp. 111–638.
31. K. Kaufmann, H. Lane, X. Liu, and K.S. Vecchio: *Sci. Rep.*, 2021, vol. 11, p. 8172.
32. A. Wijaya, B. Eichinger, F.F. Chamasemani, B. Sartory, R. Hammer, V. Maier-Kiener, D. Kiener, M. Mischitz, and R. Brunner: *Mater. Des.*, 2021, vol. 197, 109188.
33. W. Węglewski, P. Pitchai, M. Chmielewski, P.J. Guruprasad, and M. Basista: *Int. J. Heat Mass Transf.*, 2022, vol. 188, 122633.
34. M. Gusenbauer, J. Fischbacher, A. Kovacs, H. Oezelt, S. Bance, P. Zhao, T.G. Woodcock, and T. Schrefl: *J. Magn. Magn. Mater.*, 2019, vol. 486, 165256.
35. K. Bochenek and M. Basista: *Prog. Aerosp. Sci.*, 2015, vol. 79, pp. 136–46.
36. M. Tokita: *Ceramics*, 2021, vol. 4, pp. 160–98.
37. B. Beausir and J.-J. Fundenberger: *Analysis Tools for Electron and X-ray diffraction, ATEX-software*, 2017, Université de Lorraine - Metz.
38. P. Singh and P. Ramakrishnan: *KONA Powder Part. J.*, 2014, vol. 14, pp. 16–30.
39. S. Nosewicz, J. Rojek, M. Chmielewski, and K. Pietrzak: *Materials*, 2019, vol. 12, p. 281.
40. S. Nosewicz, J. Rojek, S. Mackiewicz, M. Chmielewski, K. Pietrzak, and B. Romelczyk: *J. Compos. Mater.*, 2014, vol. 48, pp. 3577–89.
41. J. Rojek, S. Nosewicz, K. Jurczak, M. Chmielewski, K. Bochenek, and K. Pietrzak: *Comput. Part. Mech.*, 2016, vol. 3, pp. 513–24.
42. Y.H. Dong, C.A. Wang, L.F. Hu, and J. Zhou: *Front. Mater. Sci.*, 2012, vol. 6, pp. 79–86.
43. S. Grandjean, J. Absi, and D.S. Smith: *J. Eur. Ceram. Soc.*, 2006, vol. 26(13), pp. 2669–76.
44. D. Buncianu, N. Tessier-Doyen, F. Courreges, and J. Absi: *Eur. J. Environ. Civ.*, 2017, vol. 21, pp. 1270–84.
45. K. Bakker: *Int. J. Heat Mass Transf.*, 1997, vol. 40, pp. 3503–11.
46. J. Wang, J.K. Carson, M.F. North, and D.J. Cleland: *Int. J. Heat Mass Transf.*, 2006, vol. 49, pp. 3075–83.
47. R. Landauer: *J. Appl. Phys.*, 1952, vol. 23, pp. 779–84.
48. D.S. Smith, J.M. Dosal, S. Oummadi, D. Nougouier, D. Vitiello, A. Alzina, and B. Nait-Ali: *J. Eur. Ceram. Soc.*, 2022, vol. 42, pp. 1618–25.
49. D.S. Smith, S. Fayette, S. Grandjean, C. Martin, R. Telle, and T. Tonnessen: *J. Am. Ceram. Soc.*, 2003, vol. 86, pp. 105–11.
50. J.P.M. Florez, M.B.H. Mantelli, and G.G.V. Nuernberg: *Int. J. Heat Mass Transf.*, 2013, vol. 66, pp. 868–78.



51. D.S. Smith, A. Alzina, J. Bourret, B. Nait-Ali, F. Pennec, N. Tessier-Doyen, K. Otsu, H. Matsubara, P. Elser, and U.T. Gonzenbach: *J. Mater. Res.*, 2013, vol. 28, pp. 2260–72.
52. J. Floury, J. Carson, and T.Q. Pham: *Food Bioproc Tech.*, 2008, vol. 1, pp. 161–70.
53. M. Smith, ABAQUS/Standard User's Manual, Version 6.9, Dassault Systemes Simulia Corp., 2009.
54. S. Nosewicz, J. Rojek, M. Chmielewski, and K. Pietrzak: *Adv. Powder Technol.*, 2017, vol. 28, pp. 1745–59.
55. N.W. Solis, P. Peretyagin, A. Seleznev, R. Torrecillas, and J.S. Moya: *AIP Conf. Proc.*, 2016, vol. 1785, 040074.
56. M. Chmielewski, S. Nosewicz, D. Jakubowska, M. Lewandowska, J. Mizera, J. Rojek, and P. Bazarnik: *Int. J. Refract. Hard Met.*, 2016, vol. 59, pp. 78–86.
57. S.A. McDonald, C. Holzner, E.M. Lauridsen, P. Reischig, A.P. Merkle, and P.J. Withers: *Sci. Rep.*, 2017, vol. 7(5251), pp. 1–11.
58. V. Randle, Y. Hu, and M. Coleman: *J. Mater. Sci.*, 2008, vol. 43, pp. 3782–91.
59. R.E. Lim, D.C. Pagan, J.V. Bernier, P.A. Shade, and A.D. Rollett: *Int. J. Fatigue*, 2022, vol. 156, 106614.
60. M. Yeadon, J.C. Yang, R.S. Averback, J.W. Bullard, D.L. Olynick, and J.M. Gibson: *Appl. Phys. Lett.*, 1997, vol. 71(12), pp. 1631–33.
61. R. Grupp, M. Nöthe, B. Kieback, and J. Banhart: *Nat. Commun.*, 2011, vol. 2, pp. 298–303.
62. S. Biswas, D. Schwen, H. Wang, M. Okuniewski, and V. Tomar: *Comput. Mater. Sci.*, 2018, vol. 148, pp. 307–19.
63. H.E. Exner and C. Müller: *J. Am. Ceram. Soc.*, 2009, vol. 92(7), pp. 1384–90.
64. S.H. Park and S.N. Rogak: *Aerosol. Sci. Technol.*, 2003, vol. 37(12), pp. 947–60.
65. R. Bjørk, V. Tikare, H.L. Frandsen, and N. Pryds: *J. Am. Ceram. Soc.*, 2013, vol. 96(1), pp. 103–10.
66. R. Besler, M. Rossetti da Silva, M. Dosta, S. Heinrich, and R. Janssen: *J. Eur. Ceram. Soc.*, 2016, vol. 36, pp. 2245–53.

**Publisher's Note** Springer Nature remains neutral with regard to jurisdictional claims in published maps and institutional affiliations.